

# A comparison of National Water Model retrospective analysis snow outputs at snow telemetry sites across the Western United States

Irene Garousi-Nejad  | David G. Tarboton 

Department of Civil and Environmental Engineering, Utah Water Research Laboratory, Utah State University, Logan, Utah, USA

## Correspondence

Irene Garousi-Nejad, Department of Civil and Environmental Engineering, Utah Water Research Laboratory, Utah State University, Logan, UT, USA.  
Email: irene.garousi@usu.edu

## Funding information

National Science Foundation, Grant/Award Numbers: ACI-1548562, OAC-1664061, OAC-1664119; Utah Water Research Laboratory (Graduate Student Research Assistantship for Irene)

## Abstract

This study compares the US National Water Model (NWM) reanalysis snow outputs to observed snow water equivalent (SWE) and snow-covered area fraction (SCAF) at snow telemetry (SNOTEL) sites across the Western United States. SWE was obtained from SNOTEL sites, while SCAF was obtained from moderate resolution imaging spectroradiometer (MODIS) observations at a nominal 500 m grid scale. Retrospective NWM results were at a 1000 m grid scale. We compared results for SNOTEL sites to gridded NWM and MODIS outputs for the grid cells encompassing each SNOTEL site. Differences between modelled and observed SWE were attributed to both model errors, as well as errors in inputs, notably precipitation and temperature. The NWM generally under-predicted SWE, partly due to precipitation input differences. There was also a slight general bias for model input temperature to be cooler than observed, counter to the direction expected to lead to under-modelling of SWE. There was also under-modelling of SWE for a subset of sites where precipitation inputs were good. Furthermore, the NWM generally tends to melt snow early. There was considerable variability between modelled and observed SCAF as well as the binary comparison of snow cover presence that hampered useful interpretation of SCAF comparisons. This is in part due to the shortcomings associated with both model SCAF parameterization and MODIS observations, particularly in vegetated regions. However, when SCAF was aggregated across all sites and years, modelled SCAF tended to be more than observed using MODIS. These differences are regional with generally better SWE and SCAF results in the Central Basin and Range and differences tending to become larger the further away regions are from this region. These findings identify areas where predictions from the NWM involving snow may be better or worse, and suggest opportunities for research directed towards model improvements.

## KEYWORDS

MODIS, National Water Model, Noah-MP, remote sensing, SNOTEL, snow parameterization, snow water equivalent, snow-covered area fraction

This is an open access article under the terms of the Creative Commons Attribution License, which permits use, distribution and reproduction in any medium, provided the original work is properly cited.

© 2022 The Authors. *Hydrological Processes* published by John Wiley & Sons Ltd.

## 1 | INTRODUCTION

Accurate water supply forecasts will become increasingly crucial as western populations grow and demand more water, and as operational agencies have to manage water under global environmental change (Bhatti et al., 2016; Gergel et al., 2017; Li et al., 2017; Livneh & Badger, 2020; Mote, 2003; Mote et al., 2005; Regonda et al., 2005; Stewart et al., 2004, 2005). Many scientific challenges in understanding and preparing for global environmental change rest upon our ability to predict streamflow and snowmelt quantity, timing, and spatial patterns that are important for decision making in water-sensitive sectors. In the United States, the National Weather Service (NWS) of the National Oceanic and Atmospheric Administration (NOAA) is responsible for short- and long-term streamflow predictions across the United States. Prior to 2016, NWS operational forecasts were limited to forecasts from NWS River Forecast Centers (RFC) at about 4000 forecast points. These were produced predominantly using the Sacramento soil moisture accounting model (SAC-SMA) to simulate runoff production and SNOW-17 model to simulate snowpack and snowmelt, within the Advanced Hydrologic Prediction System (AHPS, <https://water.weather.gov/ahps/rfc/rfc.php>) modelling infrastructure (McEnery et al., 2005).

While Franz et al. (2008) showed that SNOW-17 performed well over the Reynolds Creek Experimental Watershed located in south-western Idaho, other studies found limitations such as being unable to capture snowmelt timing precisely due to its simple conceptual framework, its inability to represent spatial variability of land properties, and its dependence on extensive calibration for each basin using historical data (Lundquist & Flint, 2006; Shamir et al., 2006; Zalenski et al., 2017). Furthermore, a National Research Council committee identified a gap between what is now considered state-of-the-art modelling capabilities and those used in AHPS (National Research Council, 2006). It concluded that the NWS needs to incorporate more advanced hydrologic science into their hydrologic models.

The increasing availability of distributed geographic data and computer power has made it possible to develop national/continental scale, physically-based, and distributed models. In 2016, NOAA's Office of Water Prediction implemented the National Water Model (NWM) as a physically-based distributed model based on the Weather Research and Forecasting Model Hydrological modelling system (WRF-Hydro) framework (Gochis, Barlage, Cabell, Casali, et al., 2020) to provide nationally consistent operational hydrologic forecasting capability. The main goals of the NWM were to provide forecast streamflow, produce spatially continuous countrywide estimates of hydrologic states (soil moisture, snowpack, etc.), and to implement a modelling architecture that permits rapid infusion of new data and science.

The NWM provides hourly flow forecasts at about 2.7 million locations in the United States. In addition to the increased number of forecast locations, another advantage of the NWM is that it utilizes a specific configuration of the physically-based Noah-MultiParameterization (Noah-MP) land surface model to represent the land-atmosphere interactions including snow processes. There have

been several studies evaluating results from the NWM. For instance, Viterbo et al. (2020) evaluated the prediction of flooding in NWM streamflow forecasts. They found that errors were due to both meteorological input errors as well as hydrologic process representation. In another study, Lahmers et al. (2019) improved the performance of WRF-Hydro configured as NWM version 1.1 by implementing a conceptual channel infiltration function into the model architecture. They concluded that accounting for channel infiltration loss in the semi-arid Western United States improves the streamflow behaviour simulated when the model is forced with high-resolution precipitation input. However, we are not aware of a systematic and thorough evaluation of the NWM snow outputs.

The NWM (Gochis, Barlage, Cabell, Dugger, et al., 2020) has been running in NWS operations since 2016 to support operational flood forecasts. The latest operational version, version 2.0, was implemented in June of 2019. Prior to this operational deployment, the NWM version 2.0 retrospective analysis data were generated (by the NWM team) for investigations into the performance of the NWM. These are publicly available in Google Cloud Storage (National Weather Service, 2019).

These retrospective analysis results contain output from a 26-year simulation (January 1993 through December 2018), hereafter is referred to as NWM-R2. The meteorological forcing data used for the version-2 retrospective analysis configuration was drawn from the North American Land Data Assimilation System II (NLDAS2) datasets, a gridded product with spatial resolution of 1/8th-degree and hourly temporal resolution. The non-precipitation forcing fields in NLDAS2 are from the analysis fields of the National Centers for Environmental Prediction (NCEP)/North American Regional Reanalysis (NARR), that is, a retrospective dataset, while the precipitation is from the gage-based NCEP/Climate Prediction Center (CPC). As a pre-processing step, the NWM team downscaled the NLDAS2 data and applied a mountain mapper (Hou et al., 2014) adjustment to the precipitation data to adjust the values for climatological variation due to topography and wind directions (RafieeiNasab et al., 2020). The result forcing dataset is a 1 km spatial resolution data layer for each hour which contains incoming short- and longwave radiation, specific humidity, air temperature, surface pressure, near surface wind, and precipitation rate. In terms of snow, outputs include gridded snow water equivalent (SWE), the amount of water stored in a snowpack, and the snow-covered area fraction (SCAF).

Across the Western United States, snow is observed at 808 snow telemetry (SNOTEL) sites that provide data intended to quantify snow and inform water supply forecasts. Illustrative comparisons of NWM-R2 SWE to SNOTEL SWE (Figure 1) indicate that SWE is well modelled at some locations (Figure 1a) while significantly different from observations at other locations (Figure 1b). Accurate modelling of SWE is a necessary condition for accurate physically-based modelling of runoff. This motivated the need, addressed in this study, to systematically evaluate the performance of NWM-R2 simulations of SWE and SCAF against available SNOTEL measurements and the moderate resolution imaging spectroradiometer (MODIS) satellite imagery to answer the following questions:

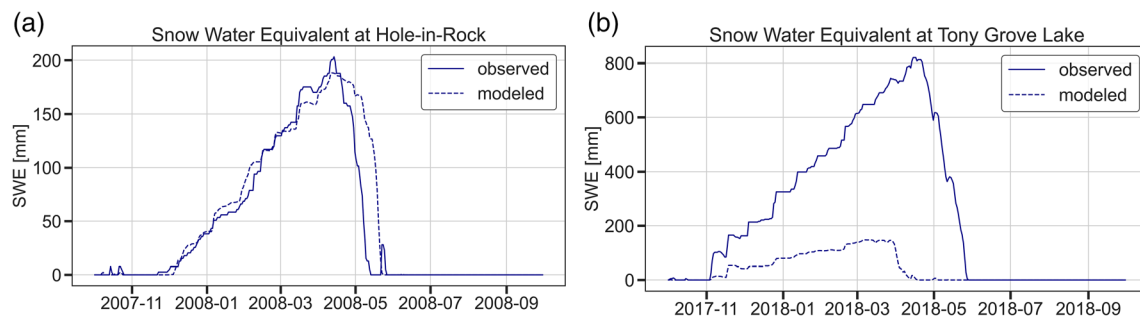


**FIGURE 1** Snow water equivalent from the National Water Model (NWM) version 2.0 reanalysis (NWM-R2) dataset compared to in situ observations at two snow telemetry (SNOTEL) sites in Utah. (a) Hole-in-Rock site (ID: 528) located at 2794 m elevation for the water year 2008. (b) Tony Grove Lake site (ID: 823) located at 2582 m elevation for the water year 2018

- How well does the NWM model simulate snowpack (in terms of SWE, SCAF, and snowmelt timing) compare to observations over the entire Western United States?
- What are the potential causes responsible for discrepancies in NWM-R2 SWE, SCAF, and snowmelt timing?
- Are these discrepancies associated with the model input errors or the snow parameterization in the model?

Answers to these questions are needed to further improve the NWM snow components, and ultimately runoff and water supply forecasts in snowmelt-dominated regions. While US based, the NWM is built using the WRF-Hydro modelling framework that has been applied worldwide, and the lessons learned from this comparison across the United States have application to the representation of snow processes in national and continental scale models throughout the world.

The following section—Section 2—first presents a summary of the NWM-R2 snow parameterization. Then, it describes the datasets used in this study, comprised of the NWM-R2 reanalysis products, SNOTEL snow observations, and MODIS imagery giving the snow-covered area fraction. Next, it presents the metrics that were used for evaluating the model results versus observations. The results section compares the NWM-R2 SWE, precipitation, air temperature, SCAF, and presence or absence of snow with observations from SNOTEL and MODIS. It also compares modelled and observed snowmelt timing. We conclude with a discussion of the uncertainties and limitations in our analysis and present ideas for future work.

## 2 | MODEL, DATA, AND EXPERIMENTAL DESIGN

The study region comprises the SNOTEL sites across the Western United States (Figure 2a). The model is the NWM version 2.0 reanalysis (NWM-R2), that includes Noah-MP land surface components for snow. Data include NWM-R2 inputs and outputs, in situ measurements, and remotely sensed data from MODIS for water years 2008–2018. NWM-R2 inputs that we used in our analysis were hourly NLDAS2-based precipitation, hourly NLDAS2-based air

temperature, and elevation—derived from the 30 m Digital Elevation Model (Zhang et al., 2021)—with 1 km spatial resolution. We used NWM-R2 outputs of 3-h SWE and SCAF with 1 km spatial resolution from the land surface module. We retrieved these inputs and outputs for NWM grid cells containing SNOTEL sites based on the nearest neighbour approach. In situ measurements comprised daily precipitation, daily air temperature, elevation, and daily SWE from SNOTEL. Remotely sensed MODIS daily snow-covered areas with nominal 500 m spatial resolution were from the MODIS sensor. The model, in situ, and remotely sensed datasets thus have different spatial resolutions (Figure 2b). The difference in scale is a potential source of uncertainty in our comparative analysis, and needs to be recognized in interpretation. There are small differences in elevation between SNOTEL (point elevations) and NWM-R2 (1 km grid elevations), that may impact temperature comparisons due to lapse rate effects, but there does not appear to be any significant bias (Figure 2c).

### 2.1 | NWM-R2 snow parameterization (Noah-MP) and snow reanalysis products

The NWM-R2 uses a particular configuration of Noah-MP (Table 1) as the land surface model to simulate snow processes as a one-dimensional vertical column over 1 km spatial resolution grid cells with no representation of any lateral snow processes within a grid cell. Details of the NWM-R2 are given in WRF-Hydro version 5.1.1 documentation (Gochis, Barlage, Cabell, Casali, et al., 2020) and the code (Gochis, Barlage, Cabell, Dugger, et al., 2020). WRF-Hydro version 5.1.1 is the WRF-Hydro version used in NWM-R2. However, (Gochis, Barlage, Cabell, Casali, et al., 2020) does not describe details of the snow parameterization. Instead reference is made to the Noah-MP technical description (Yang et al., 2011) and associated paper (Niu et al., 2011). Here we have summarized key features of the snow parameterization that pertain to the interpretation of our results. The focus in this paper is on NWM-R2 results, practically, amounts to a large-scale test of Noah-MP as configured for use in the NWM.

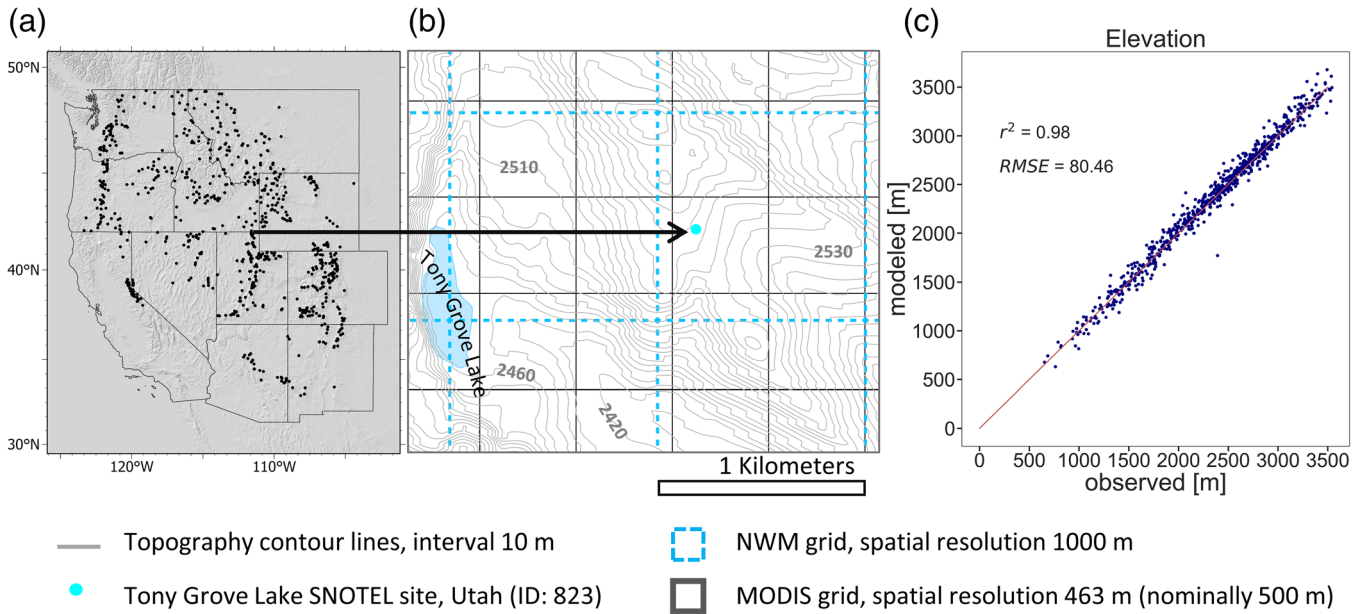


**FIGURE 2** (a) Snow telemetry (SNOTEL) sites (734 black dots) across the Western United States. (b) Illustrative relationship of Tony Grove Lake, Utah SNOTEL site (ID: 823), within National Water Model (NWM) grid cells with a spatial resolution of 1 km and moderate resolution imaging spectroradiometer (MODIS) grid cells with a spatial resolution of 463 m (nominally 500 m). (c) NWM grid cell elevation versus elevation reported for SNOTEL sites (observed). Note that there are four MODIS grid cells that have their centroid within each single NWM grid cell

### 2.1.1 | Snowfall

The separation of precipitation into rainfall or snowfall is based on Jordan's (1991) algorithm that uses near surface air temperature thresholds (Equations 1 and 2).

$$f_{p,ice} = \begin{cases} 1.0 & T_{frz} + 0.0 \leq T_{sfc} \leq T_{frz} + 0.5 \\ 1.0 - (-54.632 + 0.2 \times T_{sfc}) & T_{frz} + 0.5 \leq T_{sfc} \leq T_{frz} + 2.0 \\ 0.6 & T_{frz} + 2.0 \leq T_{sfc} \leq T_{frz} + 2.5 \\ 0.0 & T_{frz} + 2.5 \leq T_{sfc} < T_{frz} + 2.5 \end{cases} \quad (1)$$

$$\begin{aligned} \text{rain} &= P \times (1 - f_{p,ice}) \\ \text{snow} &= P \times f_{p,ice} \end{aligned} \quad (2)$$

where  $f_{p,ice}$  is the snow fraction in precipitation,  $T_{sfc}$  (K) is the surface air temperature,  $T_{frz}$  (273.16 K) is freezing/melting point, and  $P$  ( $\text{mm s}^{-1}$ ) is the input precipitation. Freshly fallen snow density ( $\rho_{fs}$  [ $\text{kg m}^{-3}$ ]) is calculated using Equation (3), based on Hedstrom and Pomeroy (1998).

$$\rho_{fs} = \min\left(120, 67.92 + 51.25e^{\left(\frac{T_{sfc} - T_{frz}}{2.59}\right)}\right) \quad (3)$$

### 2.1.2 | Vegetation and snow interception

In Noah-MP, a single-layer vegetation canopy model characterizes the fraction covered by vegetation (FVEG) in each model grid cell. Since the Noah-MP dynamic vegetation option is set off in NWM-R2, the model

uses the maximum vegetation fraction from the leaf area index (LAI) table as FVEG. If a model grid has a FVEG > 0 and a snow depth greater than 0.025 m (from initial conditions or the last time step), the model computes the fraction of canopy buried by snow based on the snow depth and the canopy height. Then, the model uses this fraction to adjust the LAI and stem area index (SAI), which are used in the snow interception model. The snow interception model allows for both liquid water and ice to be present on the vegetation canopy; and includes loading/unloading of snowfall, melting of intercepted snow and refreezing of the meltwater, frost/sublimation of canopy-intercepted snow, and dew/evaporation. The model solves the canopy liquid water balance (Equation 4) and ice balance (Equation 5) based on Niu and Yang (2004).

$$\frac{\partial M_{liq}}{\partial t} = R_{intr} + (R_{dew} - R_{eva}) + (R_{melt} - R_{frz}) \quad (4)$$

$$\frac{\partial M_{ice}}{\partial t} = (R_{load} - R_{unload}) + (R_{frost} - R_{sub}) + (R_{frz} - R_{melt}) \quad (5)$$

where  $M_{liq}$  ( $\text{kg m}^{-2}$ ) is the storage of liquid water in the canopy, and  $R_{intr}$  ( $\text{kg m}^{-2} \text{s}^{-1}$ ),  $R_{dew}$  ( $\text{kg m}^{-2} \text{s}^{-1}$ ), and  $R_{eva}$  ( $\text{kg m}^{-2} \text{s}^{-1}$ ) are interception rate for rain, dew rate, and evaporation rate, respectively.  $R_{melt}$  ( $\text{kg m}^{-2} \text{s}^{-1}$ ) and  $R_{frz}$  ( $\text{kg m}^{-2} \text{s}^{-1}$ ) are melting and refreezing rates.  $M_{ice}$  ( $\text{kg m}^{-2}$ ) is the storage of ice in the canopy and  $R_{load}$  ( $\text{kg m}^{-2} \text{s}^{-1}$ ) and  $R_{unload}$  ( $\text{kg m}^{-2} \text{s}^{-1}$ ) are snow loading and unloading rates, respectively.  $R_{frost}$  ( $\text{kg m}^{-2} \text{s}^{-1}$ ) and  $R_{sub}$  ( $\text{kg m}^{-2} \text{s}^{-1}$ ) are frost and sublimation rates. Heat transported by snow and rain to the vegetation canopy layer, the vegetated ground, and non-vegetated ground is also computed; and is used later in the energy balance computation.

**TABLE 1** The Noah-MP land surface model options as defined in the National Water Model version 2.0 retrospective analysis configuration<sup>a</sup>

Code name	Long name	Physics option used
DYNAMIC_VEG_OPTION	Dynamic vegetation	4: Using monthly LAI is prescribed for various vegetation types
CANOPY_STOMATAL_RESISTANCE_OPTION	Canopy stomatal resistance	1: Ball–Berry
BTR_OPTION	Soil moisture factor for stomatal resistance	1: Noah type using soil moisture
RUNOFF_OPTION	Runoff and groundwater	3: Noah type surface and subsurface runoff (free drainage)
SURFACE_DRAG_OPTION	Surface layer drag coefficients	1: Monin–Obukhov
FROZEN_SOIL_OPTION	Frozen soil permeability	1: Using the total soil moisture to compute hydraulic properties
SUPERCOOLED_WATER_OPTION	Supercooled liquid water (or ice fraction)	1: No iteration (Form of the freezing-point depression equation)
RADIATIVE_TRANSFER_OPTION	Radiation transfer	3: Two-stream applied to vegetated fraction
SNOW_ALBEDO_OPTION	Ground snow surface albedo	2: BATS
PCP_PARTITION_OPTION	Partitioning precipitation into rainfall and snowfall	1: Jordan (1991)
TBOT_OPTION	Lower boundary condition of soil temperature	2: TBOT at ZBOT (8 m) read from a file
TEMP_TIME_SCHEME_OPTION	Snow/soil temperature time scheme (only layer 1)	3: Semi-implicit; flux top boundary condition, but FSNO for TS calculation
GLACIER_OPTION	Glacier treatment	2: Ice treatment more like original Noah
SURFACE_RESISTANCE_OPTION	Surface resistant to evaporation and sublimation	4: For non-snow; rsurf = rsurf_snow for snow (set in MPTABLE)

Abbreviations: BATS, biosphere–atmosphere transfer scheme; LAI, leaf area index.

<sup>a</sup>Based on Gochis, Barlage, Cabell, Casali, et al. (2020) and Gochis, Barlage, Cabell, Dugger, et al. (2020).

### 2.1.3 | Snow-covered area and snow albedo

Noah-MP calculates SCAF based on snowpack density ( $\rho_{\text{sno}}$  [ $\text{kg m}^{-3}$ ]), snow depth ( $h_{\text{sno}}$  [m]) from initial conditions or the previous time step, snow surface roughness length ( $z_{0,g}$  [m]), density of fresh snow ( $\rho_{\text{new}}$  [ $\text{kg m}^{-3}$ ]), and a dimensionless area-depth factor ( $m$ ) that determines the curve relating SCAF and snow depth (Equation 6) as developed by Niu and Yang (2007).

$$\text{SCAF} = \tanh\left(\frac{h_{\text{sno}}}{2.5z_{0,g}\left(\frac{\rho_{\text{sno}}}{\rho_{\text{new}}}\right)^m}\right), \rho_{\text{sno}} = \frac{\text{SWE}}{h_{\text{sno}}} \quad (6)$$

In NWM-R2 calculations of snow-covered area,  $\rho_{\text{new}}$  and  $z_{0,g}$  are constants set equal to  $100 \text{ kg m}^{-3}$  and  $0.002 \text{ m}$ , respectively. However, the factor  $m$  is among the parameters that are adjusted during calibration to minimize differences between modelled and observed streamflow over calibration watersheds (Lahmers et al., 2019; RafieeiNasab et al., 2020). The functional relationship between SCAF and depth quantifies small-scale variability of snow within a computational grid element which plays an important role in the process governing snow accumulation and ablation. SCAF is used to weight the ground emissivity and ground surface resistance. It also affects the computed snow surface albedo that is modelled using the biosphere–atmosphere transfer scheme (BATS). BATS (Yang & Dickinson, 1996) models direct and diffusive radiation in visible and near-infrared bands separately accounting for fresh snow albedo, snow age, grain size growth, impurity, and solar zenith angle.

### 2.1.4 | Surface energy balance, radiation, and momentum fluxes

Shortwave radiation is modelled over the entire grid cell using a modified two-stream approximation (Niu & Yang, 2004) treating the vegetation as evenly distributed with gaps. The result is canopy-absorbed and ground-absorbed solar radiation over the grid cell. Longwave radiation, latent heat, sensible heat, and ground heat fluxes are modelled, using a tile approach that treats vegetated and bare fractions of the cell separately (Niu et al., 2011). Noah-MP treats turbulence fluxes between the snowpack, vegetation canopy, and air using Monin–Obukhov similarity theory to model atmospheric stability conditions. Stability corrections of under canopy turbulent transfer account for the strong stable condition of a warmer canopy overlying the snow surface during the melt season (Chen, Barlage, et al., 2014). Precipitation advected heat is also computed separately for the canopy vegetation, vegetated ground surface, and non-vegetated ground surface. The vegetation canopy temperature ( $T_v$ ), the vegetated ground surface temperature ( $T_{g,v}$ ), and the non-vegetated ground surface temperature ( $T_{g,b}$ ) are estimated using the Newton–Raphson method with 20 iterations. If the snow depth is greater than a specified snow depth ( $\geq 0.05 \text{ m}$ ) and the ground surface temperature ( $T_{g,v}/T_{g,b}$ ) is greater than the freezing point ( $273.16 \text{ K}$ ), the ground temperature is updated to  $(1 - \text{SCAF}) \times T_g + \text{SCAF} \times T_{\text{frz}}$ , and all turbulent fluxes are reevaluated. Finally, these radiative and turbulent fluxes are then aggregated based on the vegetated fraction (FVEG) parameter.

### 2.1.5 | Snowpack vertical discretization and snow thermal properties

The Noah-MP snow module uses up to three snow layers, depending on depth (from initial conditions or the last time step). The state variables for each layer are the mass of liquid water, mass of ice, layer thickness, and layer temperature. Snow can also exist in the model without being represented by explicit snow layers. This occurs when the total snowpack thickness is less than a specified minimum snow depth (<0.025 m). In this case, the only state variable is the mass of snow.

Snow thermal properties including partial volume of ice, partial volume of liquid water, effective porosity, bulk density (based on Lynch-Stieglitz, 1994), volumetric specific heat, and thermal conductivity are computed for each snow layer (Equations 7–12). Energy for phase change (melting/refreezing) is also computed for each layer.

$$\theta_{ice,i} = \frac{Mass_{ice,i}}{\Delta Z_i \times \rho_{ice}} \quad (7)$$

$$\theta_{e,i} = 1 - \theta_{ice,i} \quad (8)$$

$$\theta_{liquid,i} = \min\left(\theta_{e,i} \frac{Mass_{liquid,i}}{\Delta Z_i \times \rho_{water}}\right) \quad (9)$$

$$\rho_{snow,i} = \frac{Mass_{ice,i} + Mass_{liquid,i}}{\Delta Z_i} \quad (10)$$

$$C_{v,i} = C_{ice} \times \theta_{ice,i} + C_{liquid} \times \theta_{liquid,i} \quad (11)$$

$$k_i = 3.2217 \times 10^{-6} \times \rho_{snow,i}^2 \quad (12)$$

where  $\theta_{ice,i}$  ( $m^{-3} m^{-3}$ ) is partial volume ice of snow layer  $i$ ,  $Mass_{ice,i}$  ( $kg m^{-2}$ ) is snow ice mass of snow layer  $i$ ,  $\Delta Z_i$  (m) is the snow layer thickness of snow layer  $i$ ,  $\rho_{ice}$  ( $917 kg m^{-3}$ ) is ice density,  $\theta_{e,i}$  ( $m^{-3} m^{-3}$ ) is the effective porosity of snow layer  $i$ ,  $\theta_{liquid,i}$  ( $m^{-3} m^{-3}$ ) is partial volume of liquid water of snow layer  $i$ ,  $Mass_{liquid,i}$  ( $kg m^{-2}$ ) is liquid water mass of snow layer  $i$ ,  $\rho_{water}$  ( $1000 kg m^{-3}$ ) is liquid water density,  $\rho_{snow,i}$  ( $kg m^{-3}$ ) is bulk density of snow layer  $i$ ,  $C_{v,i}$  ( $J m^{-3} K^{-1}$ ) is volumetric specific heat of snow layer  $i$ ,  $C_{ice}$  ( $2.094 \times 10^6 J m^{-3} K^{-1}$ ) is specific heat capacity of ice,  $C_{liquid}$  ( $4.188 \times 10^6 J m^{-3} K^{-1}$ ) is specific heat capacity of liquid water, and  $k_i$  ( $W m^{-1} K^{-1}$ ) is thermal conductivity of snow layer  $i$ .

Heat flux between layers is calculated based on temperature gradient and thermal conductivity, and then this is used to update layer temperatures using a semi-implicit numerical scheme. When heat flux calculations result in temperatures of snow layers greater than freezing, the excess energy is used to adjust (melt or freeze) liquid water present. The change in the density of the snow with time due to destructive metamorphism, the weight of the overlying layers of snow, and melting (which dictates layer thickness) is modelled, following Anderson (1976) as a function of snow temperature (Niu et al., 2011).

### 2.1.6 | SWE and snow depth

The change in SWE is balanced by the input snowfall ( $Q_{snow}$ ) reaching the surface in forms of drip and throughfall; and output snowmelt ( $M$ ), snow sublimation, and snow frost (both expressed as  $E$  in Equation 13).

$$\frac{dSWE}{dt} = Q_{snow} - M - E \quad (13)$$

When new snowfall occurs in a time step, the snow depth and snow ice are increased based on the snow depth increasing rate and the input snowfall rate (both outputs of the snow interception module), respectively. After the depth, phase change and compaction calculations, the number of snow layers is adjusted by either combining the neighbour layers or subdividing them following Jordan (1991). If rainfall (in terms of drip and throughfall) occurs, it is added to the liquid water of the snow layer. The liquid water movement within a snow layer is added to the underlying snow layer when the liquid water content within a snow layer exceeds the layer's liquid water-holding capacity for snowpack ( $0.03 m^3 m^{-3}$ ). Finally, the liquid water of the snow layer updates after the water flows out of the layer.

### 2.1.7 | Post-processing NWM-R2 snow reanalysis products

This study used the NWM-R2's land surface model outputs, which are geospatial gridded results with a spatial resolution of 1 km and temporal resolution of 3 h. We obtained the NWM-R2 SWE (model code name: SNEQV) and SCAF (model code name: FSNO) for grid cells containing SNOTEL sites based on the nearest neighbour approach (code available at Garousi-Nejad & Tarboton, 2022d) from the NOAA Google Cloud archive using a Jupyter Notebook (code available at Tarboton & Garousi-Nejad, 2021). Then, we averaged 3-h results to daily values (code available at Garousi-Nejad & Tarboton, 2022f) to have a similar temporal resolution when comparing the NWM-R2 results with SNOTEL and MODIS observations because both these datasets produce daily data. We also obtained the hourly precipitation, hourly air temperature, and elevation input data used for NWM-R2 simulations for the selected grid cells. The WRF-Hydro team at NCAR provided precipitation and air temperature values for us as those data were not available on the Google Cloud archive. Then, we computed daily precipitation and the daily average temperature (code available at Garousi-Nejad & Tarboton, 2022f).

## 2.2 | SNOTEL

SNOTEL stations, managed by the Natural Resources Conservation Service (NRCS), generally consist of a snow pillow, an air temperature sensor, and a storage precipitation gage. Our study used the daily precipitation, air temperature, and SWE values measured at SNOTEL

sites as a reference dataset to evaluate the NWM-R2 precipitation, air temperature, and SWE. We realize that SNOTEL data must be used with some caution because the sites are mostly located in small clearings within forests protected by forest canopies, leading to differences in exposure to wind and radiation (McCreight et al., 2014). Furthermore, SNOTEL data do not undergo a high correction level (Swenson & Lawrence, 2012). In some instances, we found unrealistically high temperature values that needed to be filtered out. Nevertheless, SNOTEL data remain the only widespread in situ SWE observations available for model validation in the Western United States (Barlage et al., 2010; Clow et al., 2012; Livneh et al., 2010; Pan et al., 2003; Toure et al., 2016). We automated retrieval of the SNOTEL data by calling its Consortium of Universities for the Advancement of Hydrologic Science, Inc (CUAHSI) web service from a Jupyter Notebook script (Garousi-Nejad & Tarboton, 2022c).

## 2.3 | MODIS

The National Aeronautics and Space Administration (NASA)'s MODIS instrument launched aboard the Terra satellite in late 1999 is designed to observe and monitor Earth changes, such as snow cover. MODIS has spectral bands in the visible and near-infrared regions, nominal 500 m spatial resolution, and near-daily global coverage. The daily snow-cover gridded tile product, MOD10A1, has been used and improved over time in multiple snow studies (Aalstad et al., 2020; Bennett et al., 2019; Magand et al., 2014; Masson et al., 2018; Salomonson & Appel, 2006; Swenson & Lawrence, 2012). We used products from the current version of the MODIS snow-cover algorithm which is the collection six suite of MODIS (hereafter referred to as MODIS-C6, or just MODIS). We chose to use MODIS-C6 (Hall & Riggs, 2016) as a reference to evaluate NWM-R2 SCAF because the improvements/revisions to MODIS-C6 (i.e., accounting for the surface temperature and surface height) led to a notable increase in accuracy of snow cover detection on mountain ranges and low illumination conditions in the Northern Hemisphere during spring and summer (Riggs et al., 2017).

The MODIS-C6 snow algorithm is designed to detect snow cover based on the normalized ratio of the differences in reflectance in band 4 (centred at 0.56  $\mu\text{m}$ , visible green) and band 6 (centred at 1.64  $\mu\text{m}$ ) of the MODIS instrument with revisions applied to alleviate snow detection commission errors (reported for previous versions) for which snow detection is uncertain. The MODIS-C6 products include this ratio, the normalized difference snow index (NDSI, product name: NDSI\_Snow\_Cover) rather than snow cover. This approach allows users to have the option to estimate snow cover using the global empirical model (Equation 14) or develop region-specific models (Riggs et al., 2016). In this study, we developed a script (Garousi-Nejad & Tarboton, 2022b) run in Google Earth Engine to retrieve NDSI\_Snow\_Cover for each NWM grid cell containing a SNOTEL site. Since MODIS output is available on a 500 m grid and NWM grid cells are 1 km in size, the script averaged NDSI\_Snow\_Cover over the four MODIS grid cells that have their centroid within the NWM grid cell

(Figure 2). Valid NDSI\_Snow\_Cover values range between 0 and 100 with values above 100 indicating missing data, no decision, night, inland water, ocean, cloud, and detector saturated issues, which we masked out in Google Earth Engine. The returned MODIS images thus have spatial gaps due to this masking. We filled gaps in each image with NDSI\_Snow\_Cover from the most previous valid value (forward filling). Then, we applied the globally-determined linear model of Riggs et al. (2016) to compute MODIS SCAF from NDSI\_Snow\_Cover values (Equation 14).

$$\text{SCAF} = \min(\max[-0.01 + 1.45 \times \text{NDSI}, 0], 1) \text{ where } \text{NDSI} \in [0, 1] \quad (14)$$

In Equation (14), the MODIS SCFA is always estimated as 1 for NDSI values equal or greater than 0.7, and it changes linearly for NDSI values between 0 and 0.7.

The resulting dataset includes 2 504 102 site-days in the period of overlap between NWM-R2 and SNOTEL data (data and code used to aggregate it are available at Garousi-Nejad and Tarboton (2022e). We organized the SNOTEL sites into subgroups using Omernik Ecoregions level III (Omernik & Griffith, 2014) available from the Commission for Environmental Cooperation (<http://www.cec.org/north-american-environmental-atlas/terrestrial-ecoregions-level-iii/>) to identify regional differences in model results versus observations. The ecoregions are areas with general similarities in location, climate, vegetation, hydrology, terrain, wildlife, and land use; and have been used in multiple prior studies (Sun et al., 2019; Trujillo & Molotch, 2014).

## 2.4 | Metrics

We used several metrics to compare NWM-R2 SWE, snow covered area fraction (SCAF), precipitation ( $P$ ), and snowmelt timing against SNOTEL SWE and MODIS-C6 SCAF.

### 2.4.1 | Seasonal

- *First day of the month comparisons* were used for NWM-R2 SWE/SCAF (modelled) versus SNOTEL SWE and MODIS SCAF (observed) for months Nov-Jun.
- *Monthly precipitation and average air temperature* were also compared for these months.

These monthly comparisons let us evaluate the seasonal variability of snow in both modelled and observed datasets for data in the period of overlap between NWM-R2 and SNOTEL data.

### 2.4.2 | SWE and snow-covered area at peak SWE

- Modelled and observed SWE and SCAF were compared on the date of observed peak SWE (*same day comparison*).

- Modelled and observed peak SWE do not necessarily occur on the same date. We compared both SWE and SCAF on the separate dates where peak SWE was modelled and observed (*different day comparison*).
- Model input and SNOTEL observed total precipitation accumulated from the start of the water year, Oct 1, to the date of peak SWE were also compared.

Total precipitation was computed to assess the degree to which differences may be attributable to precipitation differences. This was done for both same day (observed peak SWE) and different day (observed and modelled peak day) comparisons. The different peak day comparison addresses the possibility that peak modelled and observed SWE may be close, but appear further apart in same day comparisons due to a timing mismatch.

### 2.4.3 | Direct (binary) comparison of snow presence or absence

- *Full snow cover*. Daily modelled SCAF taken as full snow if SCAF is  $\geq 0.95$ . Daily MODIS inferred (observed) SCAF taken as full snow if NDSI is  $\geq 0.7$ .
- *Some snow cover*. Daily SCAF taken as indicating some snow if modelled SCAF, or MODIS NDSI  $> 0.3$ .

First, we classified the snow presence or absence grid cells based on these thresholds. We then counted the number of classified grid cells for both observed and modelled datasets for each date. This was done only for grid cells locations where SNOTEL sites exist, because our scripts extracting NWM output were only run at these locations and running for all grid cells across the Western United States was computationally prohibitive.

- *Presence Absence comparison metrics* were used to indicated the degree-of-overlap between modelled and observed datasets (Horritt & Bates, 2002; Sangwan & Merwade, 2015).

The correctness metric (Equation 15) compares the total number of modelled and observed grid cells having some or full snow cover, while the fit metric (Equation 16) quantifies whether modelled and observed locations match, scaled by the total area mapped with snow (either full or some).

$$C_t = \frac{\text{Modelled}_{\text{snow}}}{\text{Observed}_{\text{snow}}} \quad (15)$$

$$F_t = \frac{\text{Modelled}_{\text{snow}} \cap \text{Observed}_{\text{snow}}}{\text{Modelled}_{\text{snow}} \cup \text{Observed}_{\text{snow}}} \quad (16)$$

where  $C_t$  and  $F_t$  are correctness and fit metrics computed for date  $t$ , respectively, and  $\text{Modelled}_{\text{snow}}$  and  $\text{Observed}_{\text{snow}}$  are grid cells

classified as snowy cells on that date. Correctness ( $C_t$ ) and Fit ( $F_t$ ) should both ideally be 1 (100%).

To account for the fact that MODIS may be interpreting vegetated grid cells as snow free and thus underestimating the snow cover (Steele et al., 2017; X. Wang et al., 2017), while NWM-R2 may have snow beneath the vegetation canopy, and that SNOTEL sites are often in openings much smaller than the cell size (1 km) in generally forested areas, we requested, and obtained from the NRCS (the agency that operates SNOTEL) a list of sites in generally open areas. We report separate metrics for these sites reported to be open. The NRCS indicated that SNOTEL sites may be open due to canopy disturbance caused by pine bark beetle damage and fire, which may have occurred during the study period, resulting in some uncertainty as to sites being open early on.

### 2.4.4 | Melt timing

- *Half melt from peak SWE date* (Clow, 2010).

The date, when half the snowpack has melted serves as a measure of melt timing somewhat robust to small fluctuations or a long period where SWE is flat near the peak. We categorized the differences between observed and modelled half melt dates as close (within 5 days), model early (the model is 6–19 days ahead of observed), model late (the model is 6–19 days after observed), and far apart (the modelled and observed differ by 20 days or more).

### 2.4.5 | Commonly used statistics

- Coefficient of determination ( $r^2$ , Equation 17) that ranges from  $-1$  to  $1$  with  $1$  indicating a perfect positive linear relationship but insensitive to proportional differences between modelled and observed data;
- Spearman's rank correlation (*Spearmanr*, Equation 18), a non-parametric measure of correlation used to measure the strength of association between modelled and observed values where value  $1$  means a perfect positive correlation;
- Root mean square error (RMSE, Equation 19), a measure of how concentrated the data are around the line of best fit;
- Nash Sutcliffe efficiency (NSE, Equation 20), a normalized statistic that determines the relative magnitude of the residual variance compared to observed values ranging from  $-\infty$  to  $1$  with  $1$  indicating observed and modelled data fits the 1:1 line; and
- Bias (*Bias*, Equation 21), the average of the difference between modelled and observed.

$$r^2 = \left[ \frac{\sum_{t=1}^N (M_t - \bar{O}_t)(M_t - \bar{M}_t)}{\sqrt{\sum_{t=1}^N (O_t - \bar{O}_t)^2 \sum_{t=1}^N (M_t - \bar{M}_t)^2}} \right]^2 \quad (17)$$



$$\text{Spearman } r = 1 - \frac{6 \sum_{t=1}^N d_t^2}{N(N^2 - 1)} \quad (18)$$

$$\text{RMSE} = \sqrt{\frac{\sum_{t=1}^N (O_t - M_t)^2}{N}} \quad (19)$$

$$\text{NSE} = 1 - \frac{\sum_{t=1}^N (O_t - M_t)^2}{\sum_{t=1}^N (O_t - \bar{O})^2} \quad (20)$$

$$\text{Bias} = \frac{\sum_{t=1}^N (M_t - O_t)}{N} \quad (21)$$

where  $M_t$  is model simulation,  $O_t$  is observation,  $N$  is the total number of simulations or observations,  $d_t$  is difference between observed and modelled rank, and the overbar indicates average.

### 3 | RESULTS

#### 3.1 | Seasonal (monthly) comparison

We compared the NWM-R2 SWE results with observations from SNOTEL and found a persistent bias in modelled SWE across most months (Figure 3). Results show that throughout the accumulation phase (November–February), the rank correlation between observed and modelled SWE increases (*Spearman r* from 0.7 to 0.8).

However, this does not necessarily indicate an acceptable model performance. The discrepancies between the observed and modelled SWE increase as snow accumulates (RMSE 21–135 mm). In the ablation phase (Mar–Jun), the rank correlation decreases, and discrepancies are highest in May (*Bias* –149 mm, RMSE 292 mm). The increasing scatter in later months (Figure 3) shows that the NWM generally performs well during the accumulation phase but simulates SWE less well during the ablation phase. Most points fall below the 1:1 line (red line). The points clustered into vertical and horizontal lines on the bottom and left axes of scatter plots in May and Jun indicate early and late modelling of complete melt out, respectively.

The comparison between the NWM-R2 SCAF and estimates from MODIS-C6 revealed that the modelled SCAF is highly uncorrelated with what is detected by satellite imagery (Figure 4). Throughout the last 3 months of the accumulation phase (December–February), the NWM results show that more than 70% of points (each representing one NWM grid cell that includes a SNOTEL site and a water year) have SCAF 0.9–1, while less than 10% have SCAF 0–0.1 (histograms in Figure 4). In contrast to the binary behaviour of the NWM-R2 SCAF, MODIS SCAF exhibits gradual increases and decreases. At most, 30% of the observed data have SCAF values ranging from 0.9 to 1 during the accumulation phase. In December, 14% of the observed data have SCAF greater than 0.9, while about 70% of modelled points have SCAF greater than 0.9. During the ablation phase (March–June), both modelled and observed datasets have relatively a similar data percentage with SCAF less than 0.1. However, the portion of the points where modelled SCAF is above 0.9 is still much more

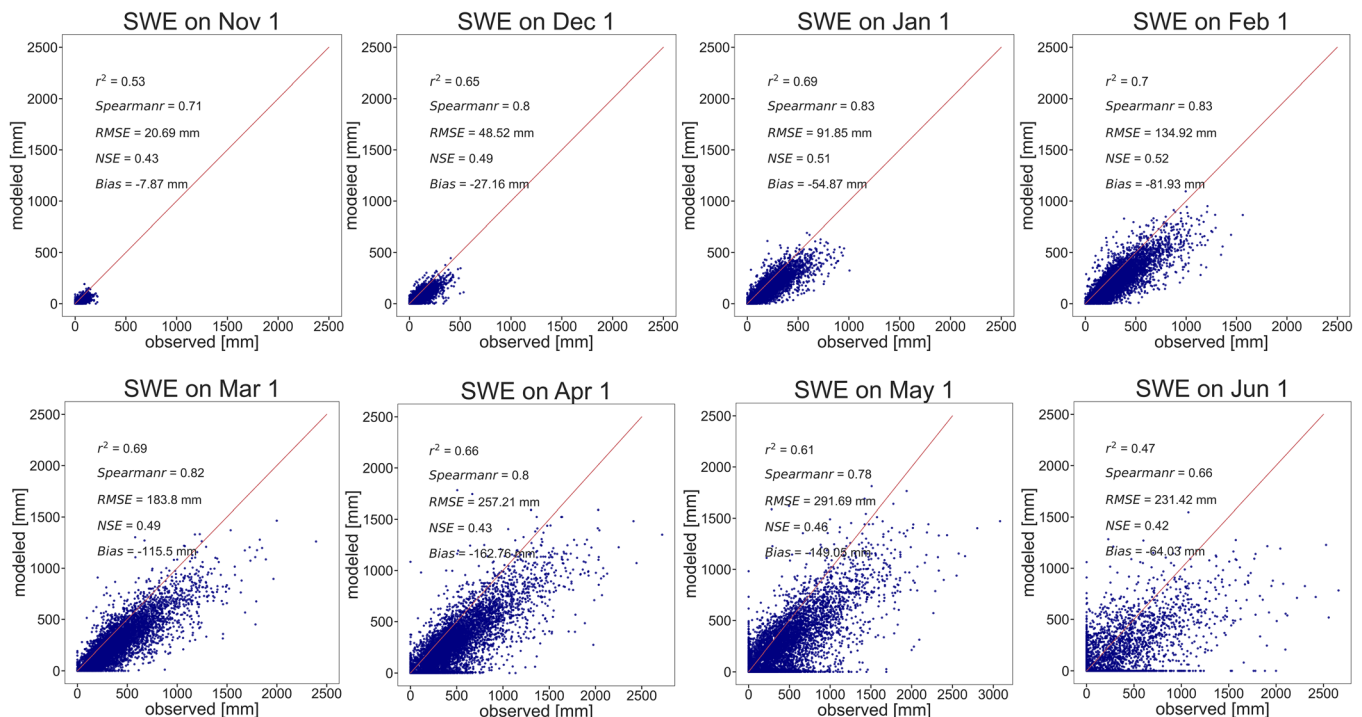


**FIGURE 3** First day of month modelled (National Water Model [NWM]-R2) versus observed (snow telemetry [SNOTEL]) snow water equivalent (SWE). Each point is a site and date in the period of overlap between NWM-R2 and SNOTEL data

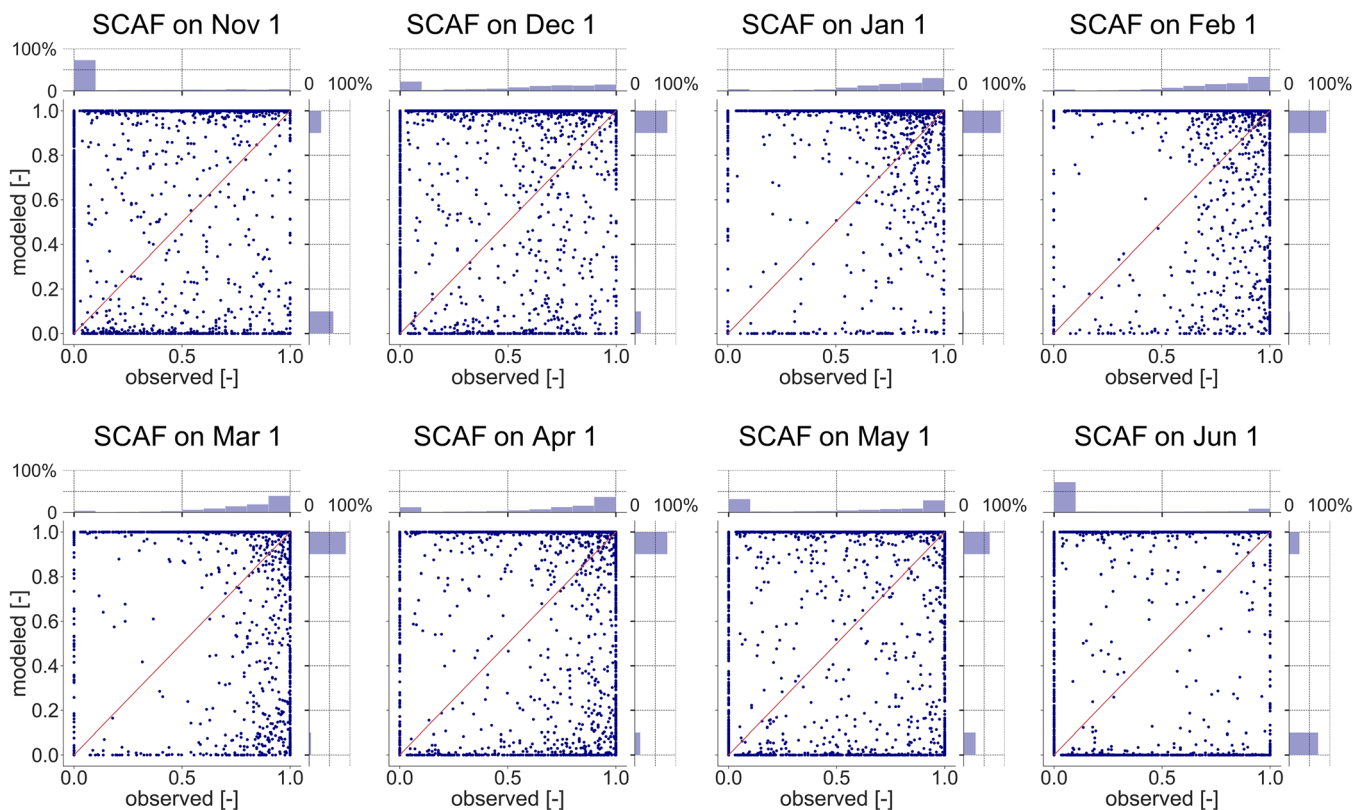


**FIGURE 4** First day of month modelled (National Water Model [NWM]-R2) versus observed (moderate resolution imaging spectroradiometer [MODIS]-C6) snow-covered area fraction (SCAF) for NWM grid cells and MODIS grid cells containing snow telemetry (SNOTEL) sites. Each point is a site and a date within the period of overlap between NWM and MODIS data. Axis histograms depict the SCAF distributions

significant (3–7 times depending on the month) than those in the observed dataset (histograms in Figure 4).

The SCAF comparisons above are only at SNOTEL sites. We did not undertake the computation needed to compare NWM-R2 and MODIS-C6 for all grid cells and dates. However, as an illustration for locations beyond SNOTEL sites NWM-R2 and MODIS-C6 SCAF maps on 1 December 2011 (Figure 5) show that while patterns are generally the same, MODIS SCAF seems less than modelled. Note that the MODIS-C6 SCAF map (Figure 5a) has gaps and cloud areas (grey) that we did not fill in from the most recent previous image with data (as described in Section 3) for this visualization. NWM-R2 SCAF covers the entire region selected based on the MODIS tiles. The visual comparison of a zoomed-in map for the region where observed SCAF were available for more than 90% of the area reveals both similarities and differences between NWM-R2 and MODIS-C6 datasets (Figure 5c,d). The NWM-R2 SCAF map for the zoomed-in area shows more white regions (i.e., SCAF values greater than 0.9), suggesting that NWM tends to overestimate SCAF compared to observations from MODIS.

Scatterplots of monthly precipitation (Figure 6) indicate model input precipitation generally less than measured at SNOTEL sites, possibly contributing to under-modelling of SWE (Figure 3). Spearman  $r$  and NSE values show an acceptable correlation between modelled and observed monthly precipitation (on average, 0.8 for both

statistics). However, the precipitation bias is larger during the accumulation phase than the ablation phase, suggesting that increased SWE scatter, in the ablation phase, is less associated with precipitation input errors than other factors during the ablation phase snowmelt.

Elevation, through orographic effects, is often suspected as a contributor to precipitation bias. However, the comparison of model input elevation (1 km grid cell) with SNOTEL point elevation (Figure 2) indicated no bias and small scatter ( $r^2 = 0.98$  in Figure 2c). There are, nevertheless, discrepancies between the NWM-R2 monthly averaged air temperature inputs and the monthly averages of the daily mean air temperature measured at SNOTEL sites (Figure 7), reported as the 24-h average of a minimum four samples per hour (US Department of Agriculture, 2011). NWM-R2 air temperatures are generally slightly below observations. This is counter to the direction needed to explain discrepancies in SWE as colder model input air temperatures should result in (1) greater fractions of precipitation as snowfall and (2) slower rather than quicker snowmelt, both processes that increase rather than decrease SWE.

The seasonal pattern of SWE and SCAF averaged across all SNOTEL site years for each specific day (Figure 8) further indicates the general under modelling of SWE and over modelling of SCAF relative to SNOTEL and MODIS observations, respectively.

Discrepancies between the seasonal pattern of SWE and SCAF are regional and somewhat different for SWE than SCAF (Figures 9

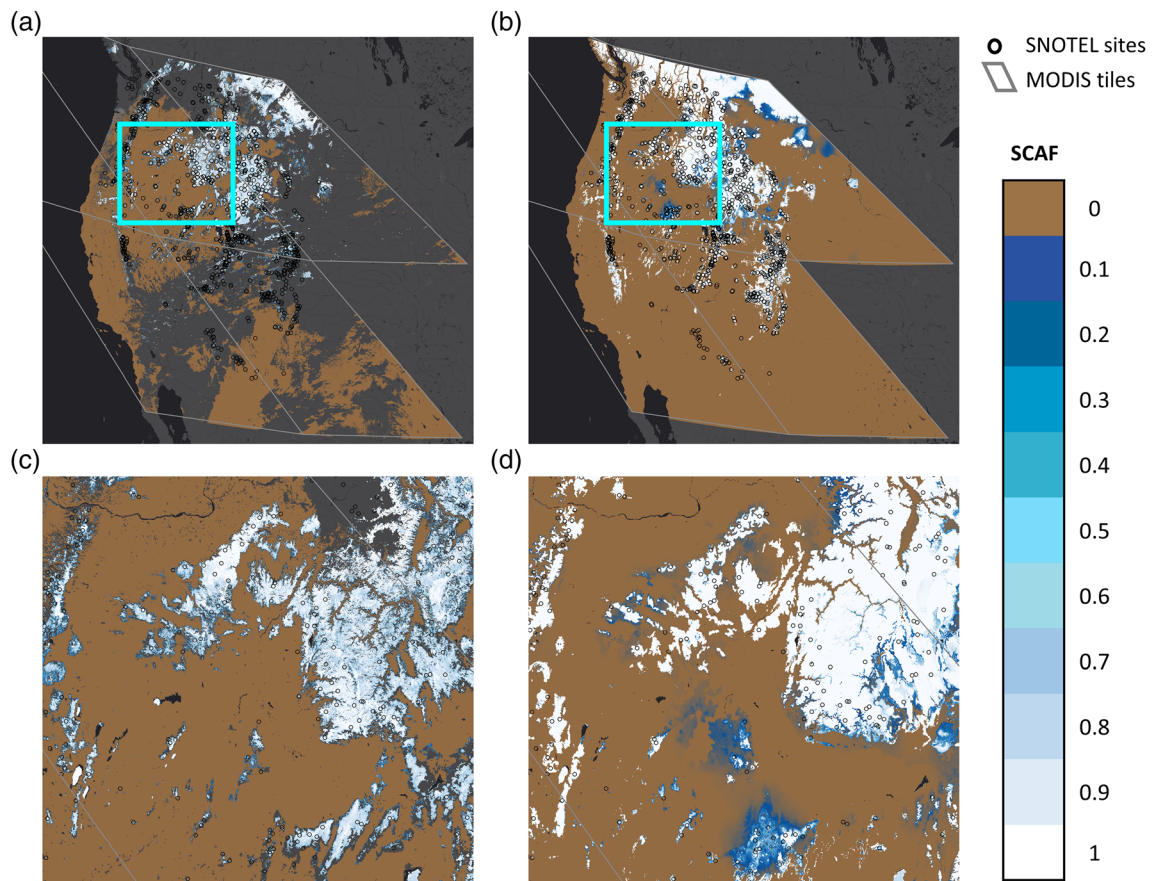


**FIGURE 5** Comparison of National Water Model (NWM)-R2 and moderate resolution imaging spectroradiometer (MODIS)-C6 snow-covered area fraction (SCAF) maps over the study region on 1 December 2011. (a) MODIS-C6 SCAF estimated from NDSI\_Snow\_Cover values of five tiles (in grey). (b) NWM-R2 SCAF outputs at 00:00 UTC masked for the MODIS-C6 tiles. (c) The zoomed-in map of MODIS-C6 SCAF for the blue box in (a). (d) The zoomed-in map of NWM-R2 SCAF for the blue box in (b)

and 10, respectively). The NWM SWE was better in the Klamath Mountains, Blue Mountains, and Central Basin and Range (region 9, 2, and 5, respectively, in Figure 9) with SWE bias differences tending to become larger further to the north and east across the study region. However, the NWM SCAF are closer to the observations in the Northern Basin and Range, Sierra Nevada, and Central Basin and Range regions (regions 12, 13, and 5, respectively, in Figure 10), with SCAF differences tending to become larger the further away regions are from the Central Basin and Range region.

### 3.2 | Observed peak SWE (same day and different day) comparison

The scatterplot of modelled versus observed SWE on the date of peak observed SWE (Figure 11a) indicates a general downward bias in modelled SWE. NWM SCAF clusters around 1 on this date (histograms in Figure 11b) while MODIS SCAF is more fractional, and similar to monthly SCAF the point comparisons are scattered and poor. Precipitation accumulated from October 1 to the date of observed peak SWE indicates model input precipitation generally less than

SNOTEL observed (Figure 11c: *Bias*  $-111$  mm, *RMSE* 212 mm). This suggests that under estimation of model precipitation inputs may be a contributor to under modelling of peak SWE. This comparison may also be influenced by the fact that observed SWE is at its peak, but modelled SWE is not.

We also compared observed and modelled peak SWE, noting that these do not necessarily occur on the same date (Figure 12). Results are similar to the observed peak SWE date comparison. Here the accumulated observed and modelled precipitation (Figure 12c) are over the accumulation period, to their respective peak SWE dates, a possible reason for increased scatter and poorer error metrics in this figure.

Under modelling of SWE is also evident when comparing the observed and modelled peak SWE for a subset of SNOTEL sites where the model precipitation is relatively close to the observed (Figure 13b: *Bias*  $-96$  mm, *RMSE* 168 mm). However, the errors are less than for the entire dataset SWE comparison. We chose this subset of sites based on the *NSE* measure between daily model input and observed precipitation being greater than or equal to 0.9 computed over the full study period. This subset shows a reduced bias (compared to the entire dataset) between the observed and modelled

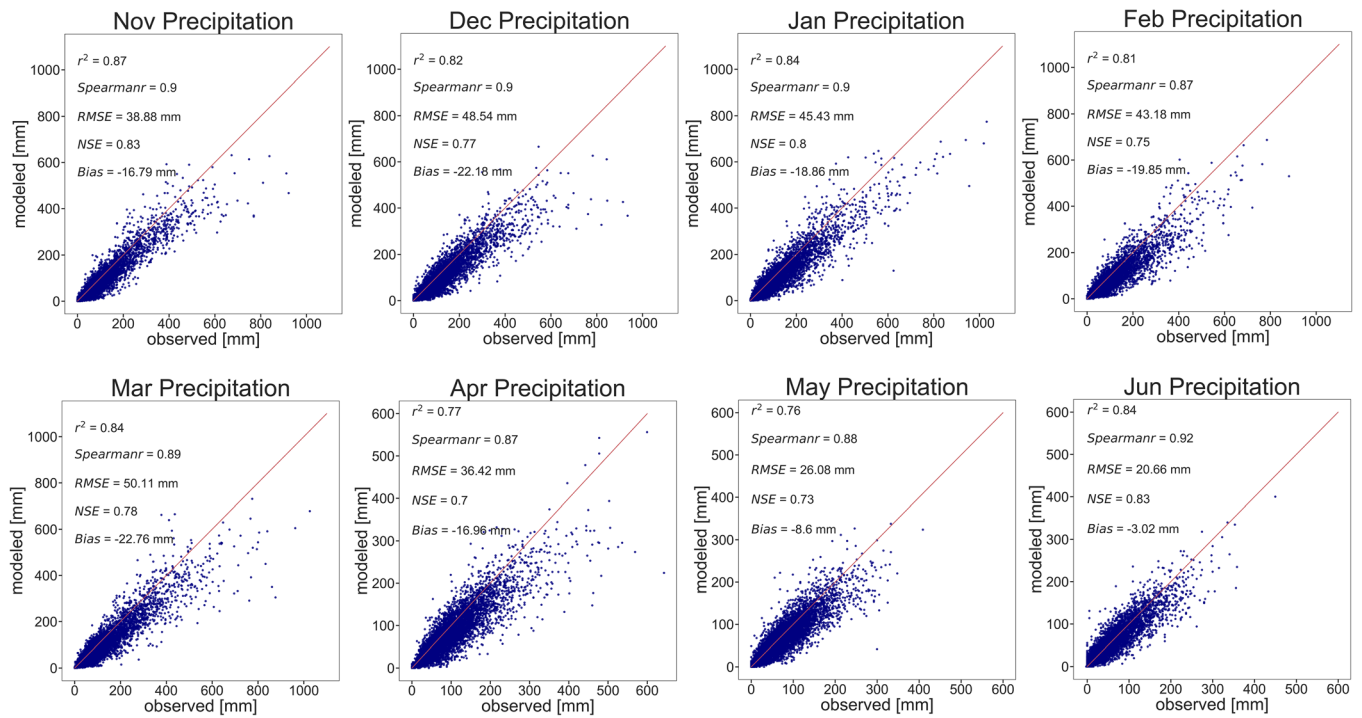


**FIGURE 6** Comparison between National Water Model (NWM)-R2 monthly precipitation input (labelled as modelled) and snow telemetry (SNOTEL) monthly precipitation (labelled as observed). Each point is a site and month in the period of overlap between NWM-R2 and SNOTEL data

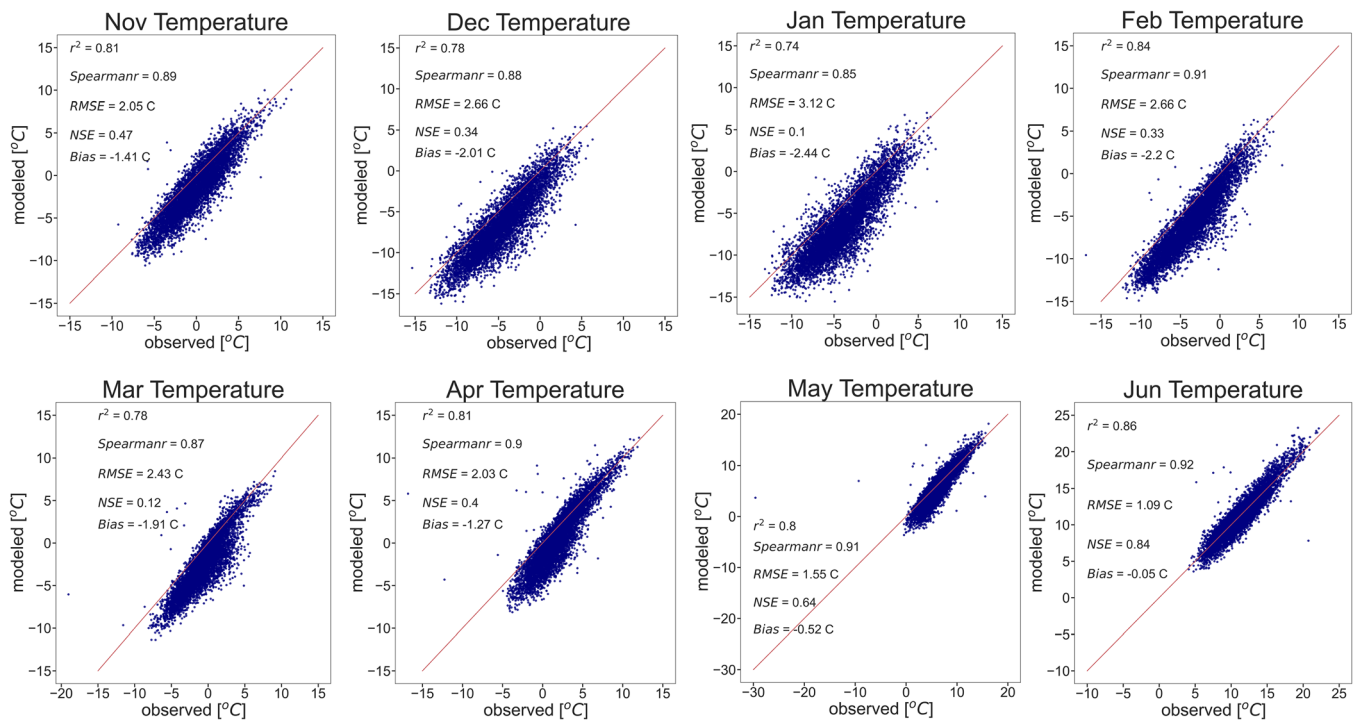
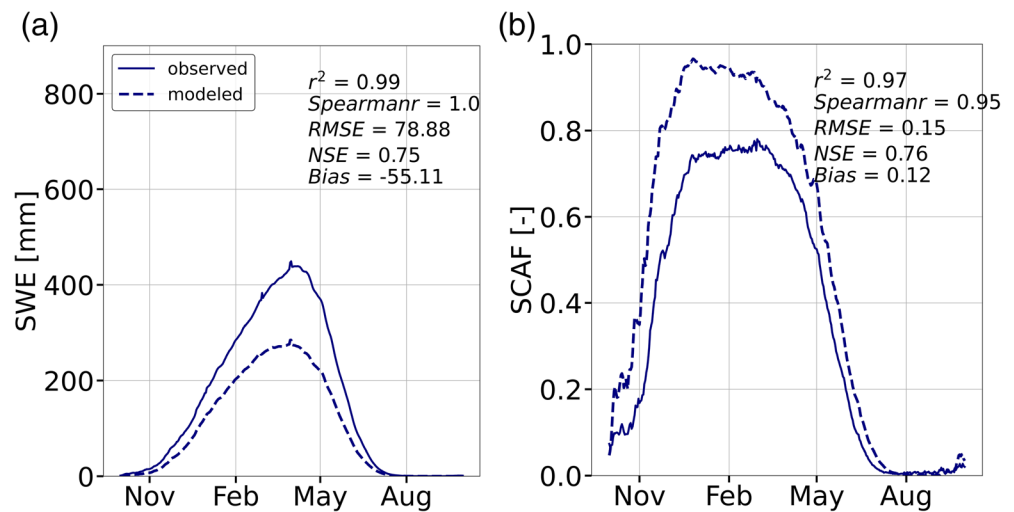


**FIGURE 7** Comparison between National Water Model (NWM)-R2 monthly average of hourly air temperature input (labelled as modelled) and snow telemetry (SNOTEL) monthly average of mean daily air temperature (labelled as observed). Each point is a site and month in the period of overlap between NWM-R2 and SNOTEL data

**FIGURE 8** Modelled and observed (a) snow water equivalent (SWE) and (b) snow-covered area fraction (SCAF) averaged across all snow telemetry (SNOTEL) sites and years for each specific day of the (water) year



precipitation accumulated from October 1 to peak observed SWE date (Figure 13a).

### 3.3 | Direct (binary) comparison of snow presence or absence

The cell by cell binary comparison of snowy grid cells at SNOTEL sites shows that this comparison does not work well for the all-snow-present condition, that is, when the observed and modelled SCAF thresholds were 0.7 and 0.95, respectively (Figure 14a). We observed that the average  $C$  for the entire period of study was 9.4 and average  $F$ , 0.11. These are poor degree of overlap statistics, and are due to the fact that MODIS never reports more than about 30% of the area as having full snow.

However, the cell by cell binary evaluation for some snow present resulted in better degree of overlap statistics (Figure 14b,  $\bar{C} = 1.47$  and  $\bar{F} = 0.50$ ). Discrepancies between the modelled and observed snowy grid cells as implied by average  $C$  ( $=1.20$ ) and  $F$  ( $=0.64$ ) were even less when we only focused on the 62 SNOTEL sites (about 8% of all sites) reported as open (Figure 14c). Table 2 summarizes fit metrics for the snow cover binary comparison.

### 3.4 | Melt timing comparison

For 68% of the site years analysed, the modelled half melt date was earlier than observed. When further classified based on whether modelled half melt dates were close, ahead, behind or far apart from observed melt dates (Figure 15a) we observe that the NWM half melt date was greater than 20 days from observed half melt date, for 34% of the site years, and off by 6 days or more for 75% of site years. For those site years where the difference was between 5 and 20 days, a greater percentage had the model melting ahead, than behind the observed. The site years that have modelled half melt date ahead of observed tend to have lower modelled half melt date SWE (which is by definition half the peak SWE) than observed (Figure 15b).

## 4 | DISCUSSION

The seasonal pattern of SWE and SCAF averaged across all SNOTEL site-years shows that NWM generally under-estimates SWE and over-estimates SCAF relative to SNOTEL and MODIS observations, respectively. These discrepancies vary regionally with relatively better SWE results in the Arizona/New Mexico Mountains, Blue Mountains, and Central Basin and Range ecoregions; and better SCAF results in the Central Basin and Range and Sierra Nevada ecoregions tending to become larger the further away regions are from the Central Basin and Range. There are several sources of uncertainties in our comparisons that need to be pointed out. The spatial scale differences in different datasets is a source of uncertainty in this analysis. A point-scale measurement of SWE cannot with confidence validate the NWM-R2 grid cell value with nearest centre, particularly in forest regions (McCreight et al., 2014). We realize that using other approaches, such as bilinear or cubic interpolation of NWM grid values would give different values at each SNOTEL site, a question we did not explore. In the cell by cell comparison between NWM-R2 and MODIS-C6 datasets, the mean value of MODIS grid cells would be different if using a different number of cells, for example, nine grid cells instead of four.

Precipitation discrepancies suggest that SWE differences are partly due to discrepancies between observed precipitation (SNOTEL) and model input precipitation (adjusted NLDAS-2 RafieeiNasab et al., 2020). There are multiple possible sources of uncertainty that may lead to this difference. First, SNOTEL latitude and longitude locations may not be precise in the geographic information from SNOTEL, as, for site security, exact site locations may not be reported. This may result in selecting a non-representative 1 km NWM grid cell. Second, there may be systematic bias for gage precipitation, particularly with snowfall measurements being subject to 'under-catch' (Mote, 2003; Sun et al., 2019). However, we note that model input precipitation was typically less than measured at SNOTEL sites, indicating that if under-catch is an issue, it may be larger in the data used to produce model inputs. In NWM version 2.0, a mountain mapper adjustment has been applied to obtain input precipitation from NLDAS-2

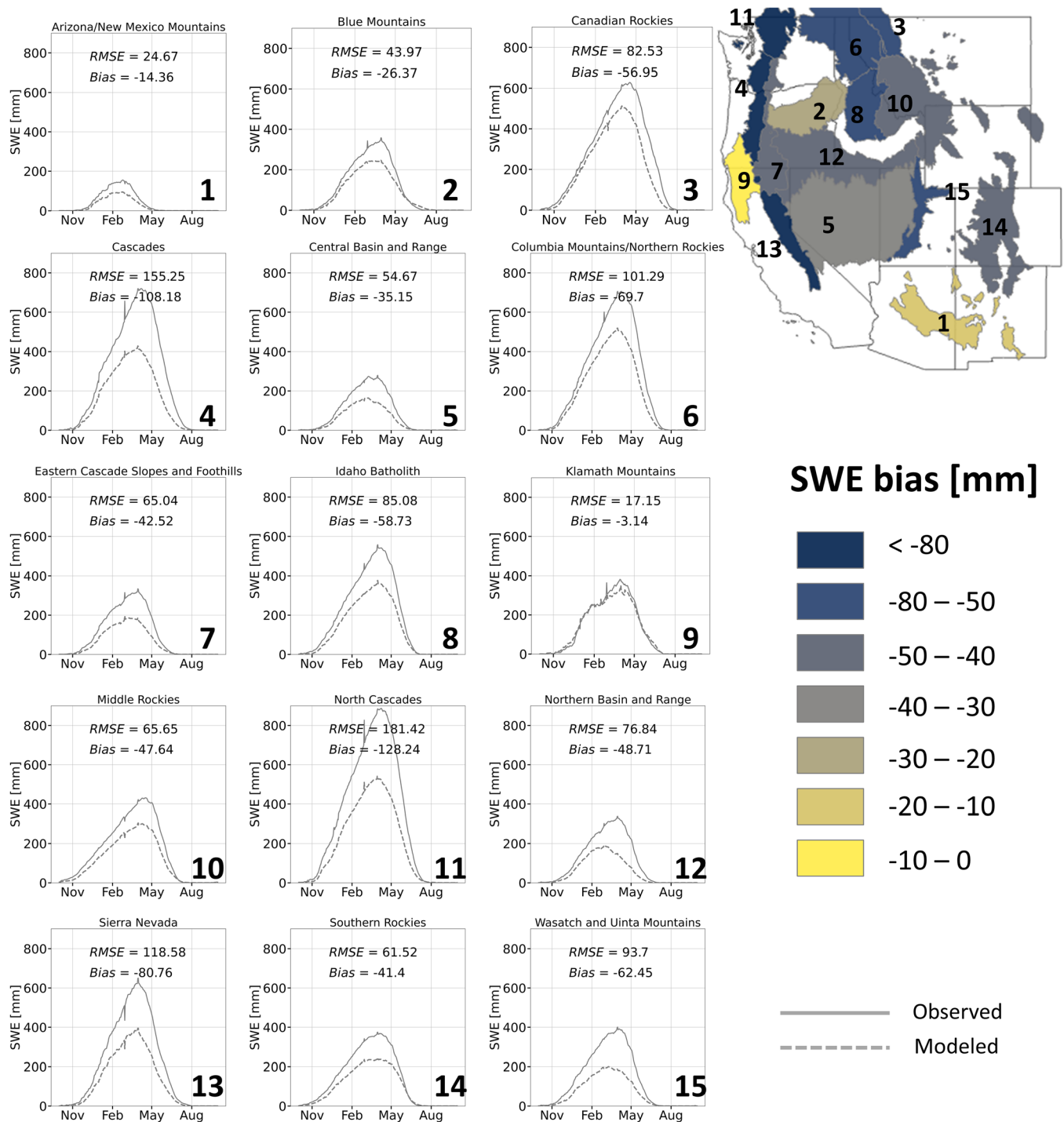


**FIGURE 9** Modelled and observed snow water equivalent (SWE) averaged across all snow telemetry (SNOTEL) sites and years for each specific day of the (water) year grouped by ecoregion. The map shows 15 Omernik ecoregions where colours represent the bias

(RafieeiNasab et al., 2020); nevertheless, there are still differences and biases compared to SNOTEL measurements that may be impacting model results. Third, SNOTEL data do not undergo a high correction level (Swenson & Lawrence, 2012). It was not uncommon to see accumulated precipitation less than SWE at SNOTEL sites (notably for stations at higher elevations), which could be due to either precipitation under-catch, or inflated SWE (Meyer et al., 2012).

This makes using this information for model comparison challenging, as the model cannot accumulate more snow than its precipitation input. This is an unresolvable difference and should be recognized as a source of uncertainty associated with the in situ measurements used in this study.

Our results show a cold (downward) bias for the model input air temperature (based on NLDAS-2) compared to SNOTEL sites'

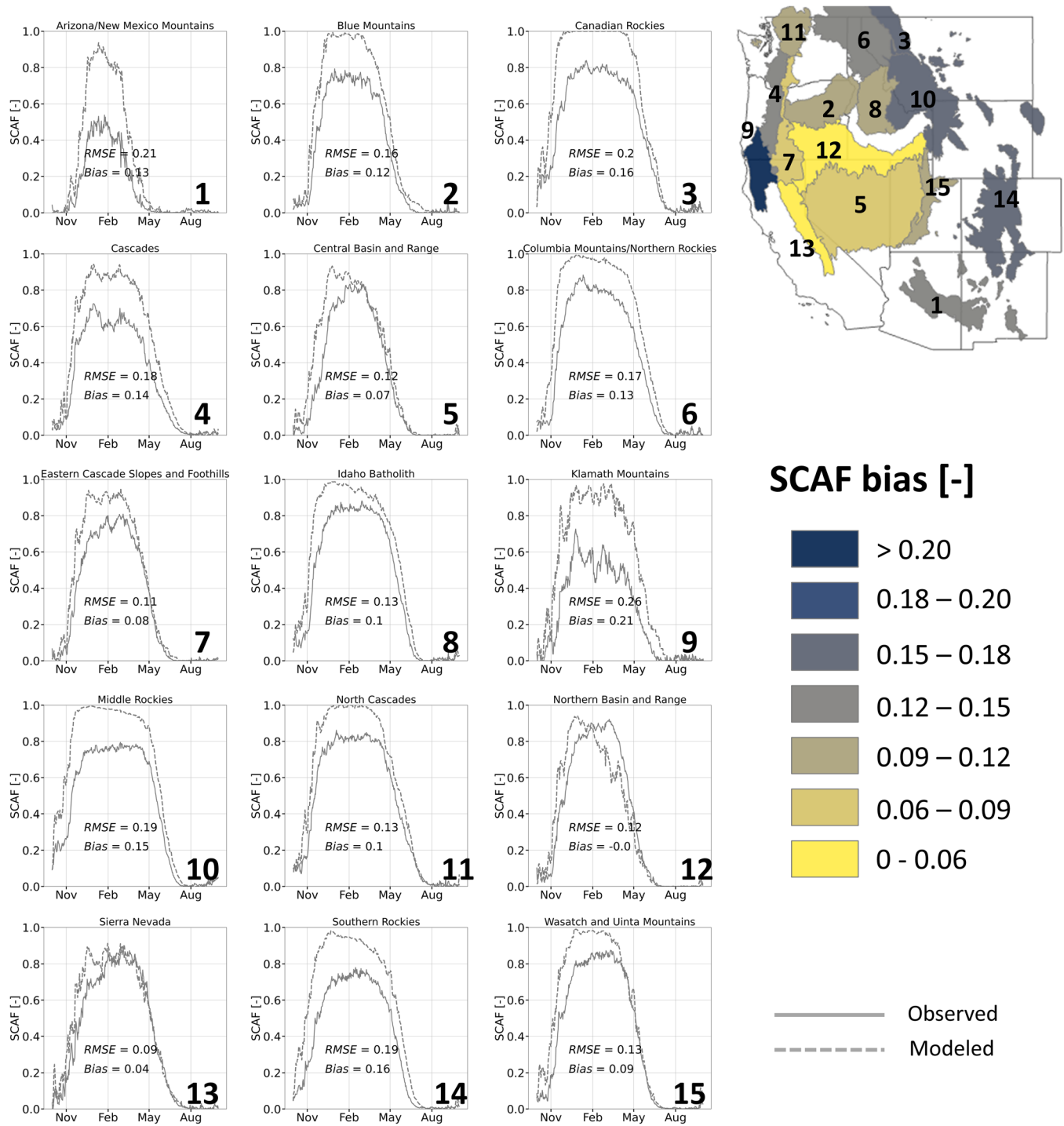


**FIGURE 10** Modelled and observed snow-covered area fraction (SCAF) averaged across all snow telemetry (SNOTEL) sites and years for each specific day of the (water) year grouped by ecoregion. The map shows 15 Omernik ecoregions where colours represent the bias

observations. This is different from Naple et al. (2020), who reported a warm (upward) bias for the NWM retrospective runs compared to the New York State Mesonet observations. The cold bias in the model temperature input is counter to the direction expected to lead to the under-modelling of SWE, a point which needs more investigation.

The discrepancies in model inputs (precipitation and air temperature in this study) are not the only potential sources for SWE

differences. Even at sites with statistically highly correlated precipitation input ( $NSE > 0.9$ ), the results indicate that some SWE bias, potentially due to other factors, still remains. This opens up the question as to whether there are other deficiencies that lead to SWE under-modelling, both due to observation and model errors. Errors in SWE measurements may occur, due to factors such as wind causing snowdrifts on the snow pillow (Meyer et al., 2012), or the small clearing

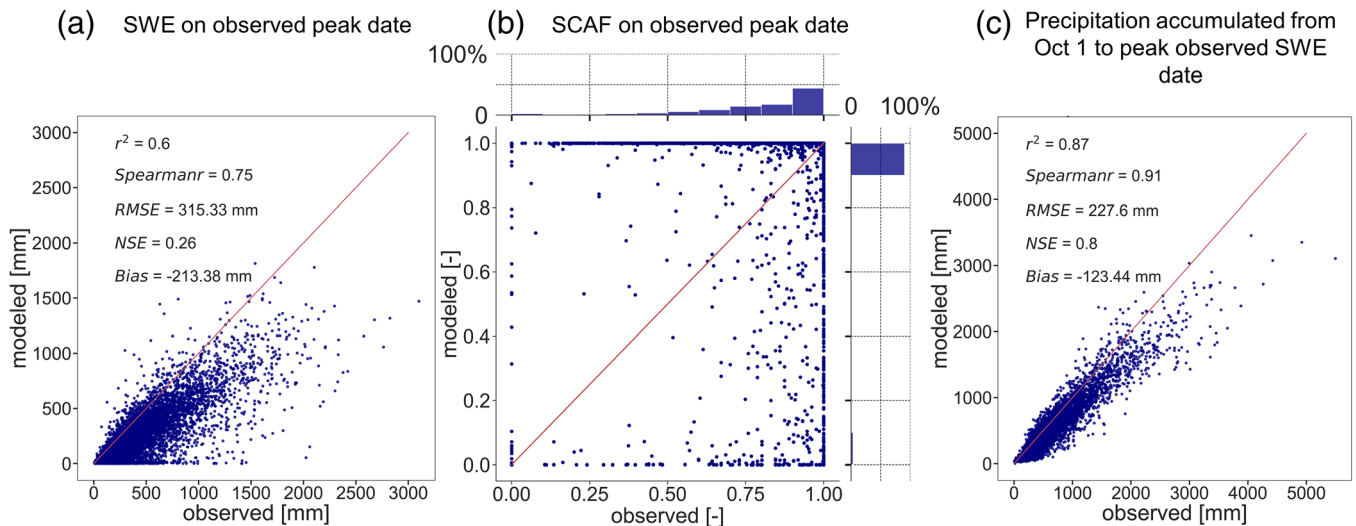


**FIGURE 11** Comparisons on date of observed peak snow water equivalent (SWE). (a) National Water Model (NWM)-R2 versus snow telemetry (SNOTEL) SWE, (b) NWM-R2 versus moderate resolution imaging spectroradiometer (MODIS)-C6 snow-covered area fraction (SCAF), and (c) NWM-R2 versus SNOTEL precipitation accumulated from 1 October to observed peak SWE date. Each point is a site and a water year (that starts 1 October) in the period of overlap between NWM-R2 and SNOTEL data

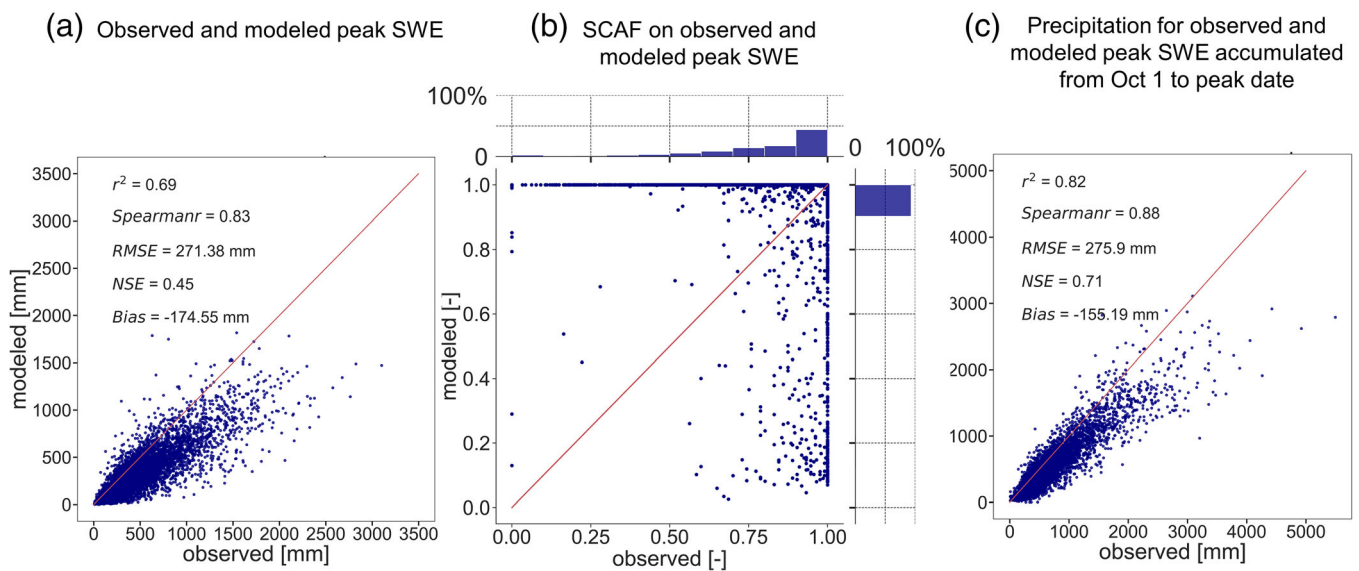


**FIGURE 12** Different date comparison on dates of observed and modelled peak snow water equivalent (SWE) (a) National Water Model (NWM)-R2 versus snow telemetry (SNOTEL) peak SWE, (b) NWM-R2 versus moderate resolution imaging spectroradiometer (MODIS)-C6 snow-covered area fraction (SCAF), and (c) NWM-R2 versus SNOTEL precipitation accumulated from 1 October to observed and modelled peak SWE dates. Each point is a site and a water year (that starts 1 October) in the period of overlap between NWM-R2 and SNOTEL data

SNOTEL site location not being representative of larger scale snowpack (McCreight et al., 2014). In the NWM land surface model (Noah-MP), the partitioning of precipitation into rainfall and snowfall, which is one of the most sensitive parameterizations in simulating cold-region hydrological processes (Loth et al., 1993), is based on Jordan's (1991) algorithm, which ignores some physical processes controlling precipitation phase by not incorporating humidity. This may lead to biases in SWE, snow depth, and snow cover fraction (Chen, Liu, et al., 2014; Harder & Pomeroy, 2014; Y. Wang

et al., 2019). Y. Wang et al. (2019) suggest that using a snow-rain partitioning scheme based on the wet-bulb temperature within Noah-MP produces more snowfall and snow mass on the ground that agrees better with ground-based snow observations, particularly over mountainous regions in the Western United States. Recently, Naple et al. (2020) shows that using the precipitation phase partition from the high-resolution rapid refresh (HRRR), in lieu of the operational method (Jordan, 1991), leads to improved snow results for the NWM version 2.0 configuration.



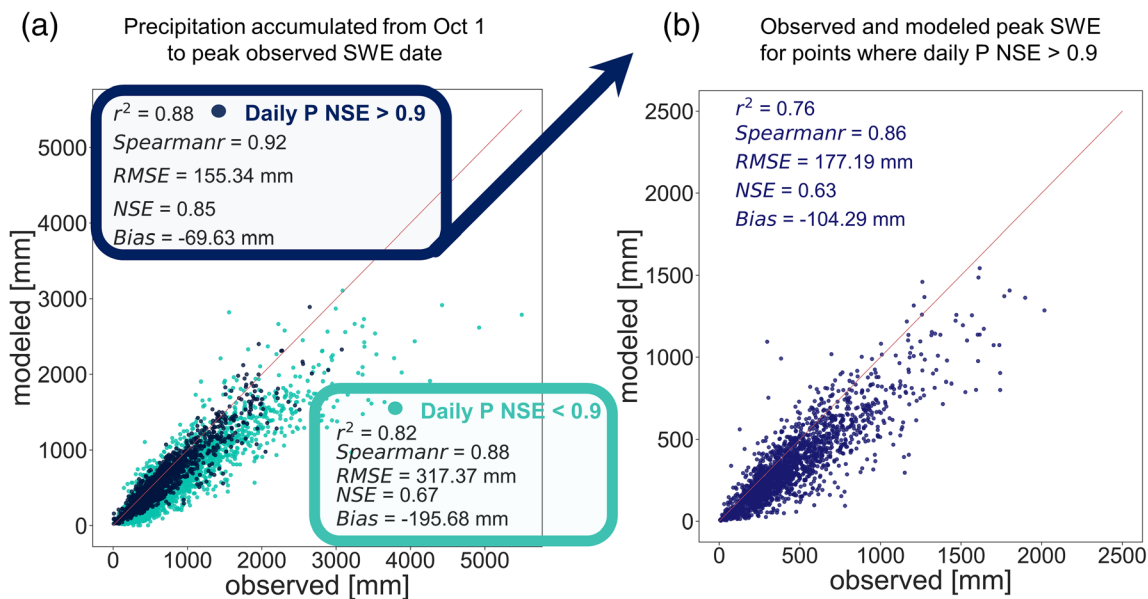


**FIGURE 13** (a) National Water Model (NWM)-R2 versus snow telemetry (SNOTEL) precipitation accumulated from 1 October to observed and modelled peak snow water equivalent (SWE) dates. This figure is similar to Figure 10a but with colours separating points into two groups. The first group (dark blue) contains points where Nash Sutcliffe efficiency (NSE) values for daily modelled versus observed precipitation are equal to or greater than 0.9. The second group (light blue) includes points where NSE values for daily modelled versus observed precipitation are less than 0.9. Statistics are reported separately for the  $NSE \geq 0.9$  and  $NSE < 0.9$  subsets. (b) NWM-R2 peak SWE versus SNOTEL peak SWE for points from (a) that have daily precipitation NSE equal to or greater than 0.9 (dark blue class)

Our results show that, on average, the NWM tends to melt snow early (6–19 days) compared to SNOTEL observation. For 75% of the site years, the modelled date of half melt from peak SWE was off by 6 days or more from the observed half melt dates, sometimes being as far apart as 2 months (for example, Magic Mountain SNOTEL site, ID: 610 in Idaho, at water year 2010). This suggests that the modelling of melt timing is somewhat problematic and there is a need to further investigate overall energy balance and snow surface temperature, possibly drawing on ideas from the Utah Energy Balance model (Mahat & Tarboton, 2014; You et al., 2014).

Overall, NWM-R2 SCAF was difficult to compare to MODIS-C6 SCAF using single SNOTEL sites and days. Some of this difficulty—manifested in the scatter in Figures 4, 11, and 12—may reflect the fact that the MODIS and NWM SCAF quantities are not really the same thing. MODIS may be interpreting vegetation as snow free (Steele et al., 2017; X. Wang et al., 2017), while NWM has snow beneath vegetation. In NWM-R2 results, the persistent low and high SCAF (<0.1 and >0.9, respectively) reflects that NWM treats SCAF as a binary metric in mountainous regions. NWM-R2 SCAF values stay near 1 with less variability between December–April for more than 70% of cases. This suggests that once the NWM grid cell (1 km spatial resolution) is more than 90% snow-covered, it is implausible for it to diverge from 1 for the rest of the accumulation phase and early ablation phase. One possible reason for this behaviour is the lack of representation of some factors affecting SCAF such as vegetation type and seasonal change, and topography. These limitations affect the accurate simulation of SCAF and SWE (Helbig et al., 2015; Magand et al., 2014; Swenson & Lawrence, 2012; Wrzesien et al., 2015).

Another possible reason for some of the differences is the lack of any representation of snow drifting processes (i.e., wind-driven redistribution of snow) in the snow model. Snow drifting increases the variability of snow depth within a grid cell, which then, when melting starts leads to intervening (non-binary 0 or 1) snow covered area fractions. This may be a factor contributing to differences in regions with modelled SCAF less than 10% while the observed SCAF are more than 50% (points along the horizontal axis of SCAF on March 1, April 1, and May 1 in Figure 4).

We recognize that the SCAF mapped from MODIS in this study also has uncertainties and limitations. First, the temporal forward filling approach that we used to fill gaps associated with clouds may miss some of the daily variability of snow cover, particularly in mountainous regions. Second, the parameters of Equation (14), which estimates SCAF from MODIS-C6 NDSI\_Snow\_Cover product, were those from Salomonson and Appel (2006) and were constant for our entire study region. Adjusting these parameters to improve the snow cover products from MODIS regionally has been suggested (Riggs et al., 2017). Third, MODIS NDSI\_Snow\_Cover grids (nominally 500 m) were averaged for 1 km NWM grid cells, using an unweighted approach in the Google Earth Engine platform. This approach selects MODIS grids whose centres fall within the target area (i.e., NWM grid cells). These scale differences may be a further source of uncertainty, compounded by the nonlinearity in Equation (14) (plateau at NDSI >0.7) having an impact on SCAF from averaged NDSI.

Results for the direct (binary) comparison of full snow cover were poor as MODIS never reports more than about 30% of the area as having full snow, while the degree-of-overlap between the modelled

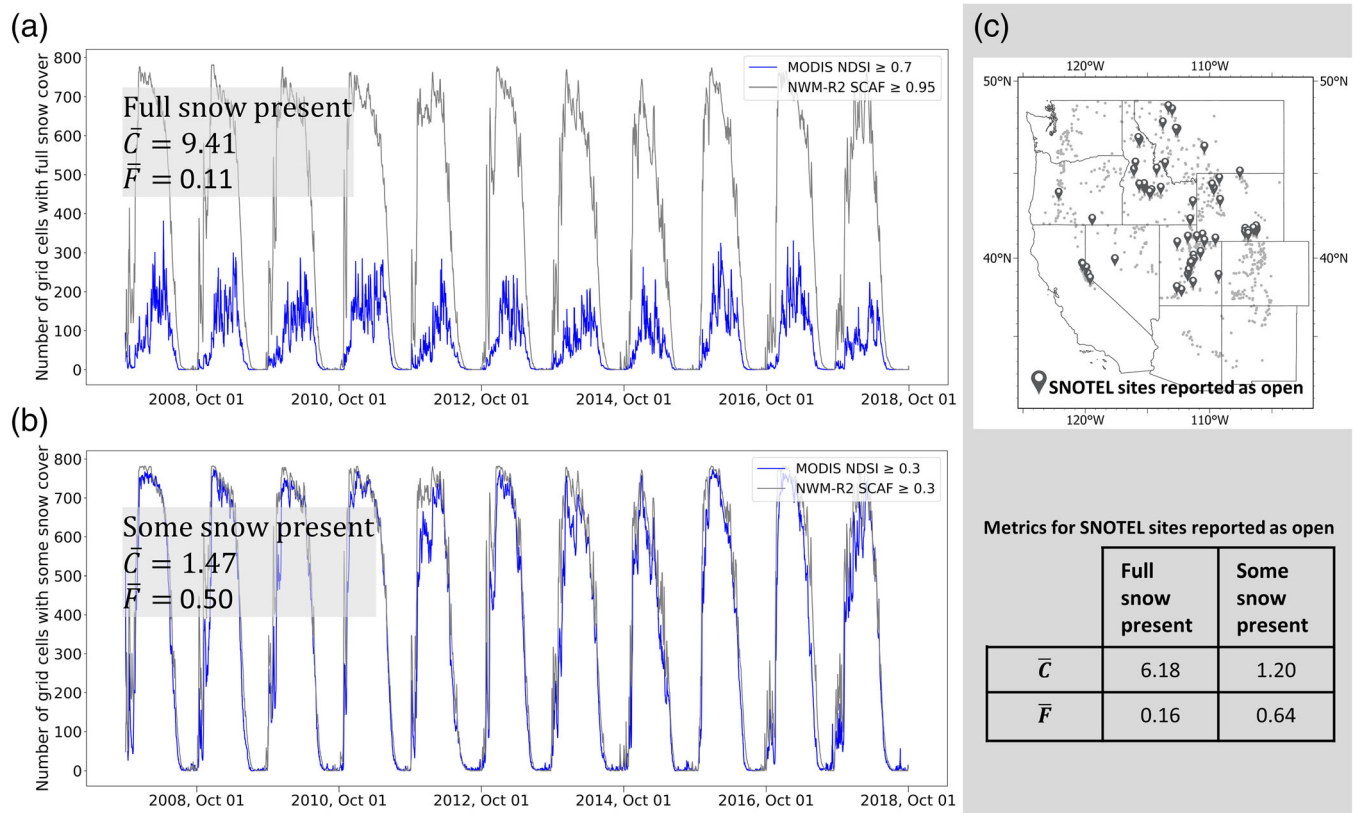


**FIGURE 14** Direct (binary) comparison of snow presence considering all 734 snow telemetry (SNOTEL) sites with (a) full snow cover and (b) some snow cover. The modelled and observed thresholds for full snow cover were National Water Model (NWM)-R2 snow-covered area fraction (SCAF)  $\geq 0.95$  and moderate resolution imaging spectroradiometer (MODIS) NDSI  $\geq 0.7$ , respectively. Lower thresholds were used for some snow cover (i.e., NWM-R2 SCAF  $> 0.3$  and MODIS NDSI  $> 0.3$ ). (c) Locations of the 62 SNOTEL sites reported as open. Average fit metrics (i.e.,  $\bar{C}$  and  $\bar{F}$ ), presented here, quantitatively evaluate the degree-of-overlap between the modelled and observed snow presence

Average metrics	(a) All 734 SNOTEL sites		(b) The 62 SNOTEL sites reported as open	
	Snow presence condition		Snow presence condition	
	Full <sup>a</sup>	Some <sup>b</sup>	Full <sup>a</sup>	Some <sup>b</sup>
$\bar{C}$	9.41	1.47	6.18	1.20
$\bar{F}$	0.11	0.50	0.16	0.64

Abbreviations: MODIS, moderate resolution imaging spectroradiometer; NDSI, normalized difference snow index; SNOTEL, snow telemetry.

<sup>a</sup>Daily modelled snow-covered area fraction (SCAF) taken as full snow if SCAF is  $\geq 0.95$ . Daily MODIS SCAF taken as full snow if NDSI is  $\geq 0.7$ .

<sup>b</sup>Daily modelled SCAF taken as some snow if SCAF is  $\geq 0.3$ . Daily MODIS SCAF taken as some snow if NDSI is  $\geq 0.3$ .

and observed results, in terms of average C and F, improved considerably when comparing cells having some snow present. We interpret this as a shortcoming of MODIS for this sort of comparison, perhaps due to the presence of vegetation. MODIS SCAF estimates may not account for snow beneath the canopy due to incapability of the sensor to see forest gaps (the snow-covered ground) through the vegetation canopy (Steele et al., 2017; X. Wang et al., 2017), while the NWM-R2 land surface model (Noah-MP) may estimate snow under the vegetation canopy in these locations. Our results show that

discrepancies between modelled and observed snowy grid cells reduce when we focus only on the SNOTEL sites reported as open. For full snow present average C improves from 9.41 to 6.18 while average F improves from 0.11 to 0.16. These are still poor, but less poor. For some snow present average C improves from 1.47 to 1.2 and average F improves from 0.5 to 0.64, making them reasonably respectable, in comparison to the ideal values of 1. This suggests that forest vegetation is a dominant contributor to the disagreement between model and MODIS observed snow cover.

**TABLE 2** Summary of average correctness ( $\bar{C}$ ) and average fit ( $\bar{F}$ ) metrics evaluated for the binary comparison of snow presence or absence when considering (a) all SNOTEL sites and (b) sites reported as open approaches

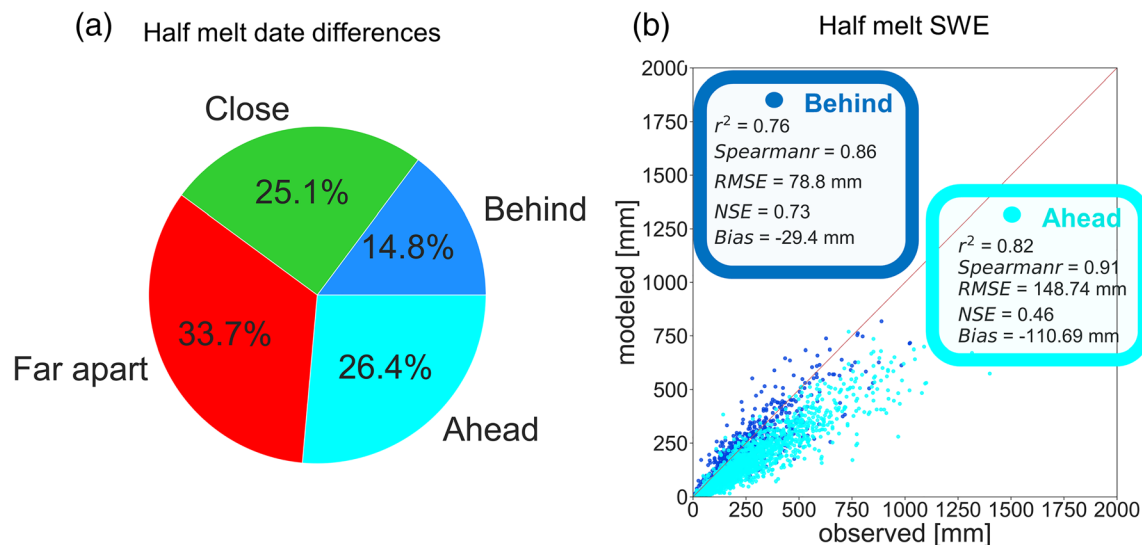


**FIGURE 15** Analysis of melt timing. (a) Classification of differences between observed and modelled dates of half melt from peak snow water equivalent (SWE). Close: Modelled and observed within 5 days of each other; behind: Modelled 6–19 days after observed; ahead: Modelled 6–19 days before observed; far apart: Modelled and observed more than 20 days apart. (b) National Water Model (NWM)-R2 SWE versus snow telemetry (SNOTEL) SWE date of half melt from peak

## 5 | CONCLUSIONS

A cell by cell comparison for sites and dates in the period of overlap between SNOTEL SWE with modelled SWE from NWM-R2 simulations, in general, shows that there is a tendency for the NWM-R2 configuration to under-estimate SWE early in the season and become progressively more biased late in the season compared to in situ observations of SWE. When aggregated across all sites and years, seasonal variations show an overall downward bias of about 55 mm with *NSE* 0.75 which varies regionally over Omernik ecoregions. SWE discrepancies are attributed to errors in inputs, notably precipitation and air temperature. The downward bias in precipitation input contributes to the downward biases in SWE and the SWE bias is persistent even when the model precipitation input is relatively close to the observed precipitation at SNOTEL sites with daily precipitation *NSE* higher than 0.9. However, the cold bias in the model temperature input is counter to the direction expected to lead to under-modelling of SWE. This needs further exploration. There is a significant variability between the MODIS SCAF and NWM SCAF in the cell by cell comparison for sites and dates in the period of overlap between model results and observations which hindered useful interpretation of these comparisons. The challenge in simulating SCAF is in part due to the model SCAF essentially being binary as it lacks representation of vegetation and topography while observations are much more fractional. They may not reflect the same physical quantity. The binary comparison of full snow presence reveals that the degree-of-overlap between the modelled and observed results still remains poor, which is possibly due to uncertainties associated with MODIS observations in vegetated areas. Results of the binary comparison of some snow presence improves

when we focus only on the SNOTEL sites reported as open (average  $C = 1.2$  and average  $F = 0.64$ ). Also, when aggregated across all sites and years, seasonal variations show an overall upward bias of 0.12 with *NSE* 0.76 which vary regionally for ecoregions. Our investigation opens some new questions for future research. First, it emphasizes the importance of having a more accurate (bias corrected) precipitation and air temperature input for the NWM. Second, there is a question as to whether, in circumstances where there is disagreement between the NWM SCAF (estimated by the Noah-MP module) and MODIS observations in the binary comparison, the SCAF parameterization should be improved or can be inferred from satellites while considering the uncertainties associated with these products. Using satellite-based snow-covered maps may potentially provide an approach or an opportunity for estimating SCAF as a way to overcome limitations associated with parameterization of SCAF in the snow model. However, there would need to be resolution of differences in definition of the physical quantity being compared. Overall, our evaluation effort identifies some challenges in the current snow parameterization within the specific settings of the Noah-MP as implemented in the NWM-R2 configuration and suggests where potential development effort should be directed in the future. It would also be helpful, for future work, to have a more comprehensive observation data set, beyond the SNOTEL sites, such as possibly Critical Zone Observatory or experimental forest sites, that include snowfall/rainfall measurements, canopy snow interception, turbulence and radiation fluxes above and below the canopy. Another opportunity is to run the model at higher resolution which would involve downscaling the forcing inputs to higher resolution. Higher-resolution remotely sensed snow-covered area (e.g., from LANDSAT satellite) could then be used for model evaluation.

## ACKNOWLEDGEMENTS

This work was supported by the Utah Water Research Laboratory for this research and National Science Foundation under collaborative grants OAC-1664061 and OAC-1664119. This work used compute allocation TG-EAR190007 from the Extreme Science and Engineering Discovery Environment (XSEDE), which is supported by National Science Foundation grant number ACI-1548562 (Townes et al., 2014). The support and resources from the Center for High Performance Computing (CHPC) at the University of Utah are gratefully acknowledged. Thanks to Arezoo RafieeiNasab of NCAR who supplied some of the National Water Model inputs for the study region and to David Gochis and the NCAR WRH-Hydro research team for encouragement and discussion. We also thank the Natural Resources Conservation Service (NRCS) staff, Danny Tappa; Jeff Anderson; Mage Hultstrand; Scott Pattee; Brian Domonkos; Dave Eiriksson; and Jordan Clayton, for their help providing us information on which SNOTEL sites are open.

## CONFLICT OF INTEREST

The authors declare no conflict of interest.

## DATA AVAILABILITY STATEMENT

All data sources used in this research are publicly available.

- The NWM-R2 are available in the NOAA Google Cloud archive at <https://console.cloud.google.com/storage/browser/national-water-model-v2?pli=1>. The precipitation and air temperature inputs prepared by the WRF-Hydro NCAR team, we have made available on HydroShare for reproducibility (Garousi-Nejad & Tarboton, 2022f). The NWM elevation dataset was obtained from <https://www.nco.ncep.noaa.gov/pmb/codes/nwprod/nwm.v2.0.4/parm/domain/> (accessed November, 30, 2020) and is saved in HydroShare for reproducibility (Garousi-Nejad & Tarboton 2022f).
- The NRCS SNOTEL data are available at <https://www.wcc.nrcs.usda.gov/snow/>
- The NASA MODIS data are available at <https://nsidc.org/data/MOD10A1/versions/6>
- The Omernik ecoregions are available at <http://www.cec.org/north-american-environmental-atlas/terrestrial-ecoregions-level-iii/>

All codes developed for this research are shared and publicly available as a collection on HydroShare (Garousi-Nejad & Tarboton, 2022a) comprised of:

- Input data and code to get the indices of the NWM grid cells containing SNOTEL sites (Garousi-Nejad & Tarboton, 2022d)
- Input data, code to retrieve the NWM-R2 inputs and outputs at SNOTEL sites (Tarboton & Garousi-Nejad, 2022)
- Input data, code and output from post-processing the retrieved NWM-R2 inputs and outputs at SNOTEL sites (Garousi-Nejad & Tarboton, 2022f)
- Input data and code to retrieve precipitation, air temperature, and SWE measurements at SNOTEL sites (Garousi-Nejad & Tarboton, 2022c)

- Input data and Google Earth Engine code to retrieve averaged MODIS-C6 NDSI snow cover at SNOTEL sites (Garousi-Nejad & Tarboton, 2022b)
- Input data, code and output from combining the NWM inputs and outputs with observations from SNOTEL and MODIS at SNOTEL sites (Garousi-Nejad & Tarboton, 2022e)
- Input data, code and output used to produce Figures 1–4 and Figures 6–15 (Garousi-Nejad & Tarboton, 2022g)

## ORCID

Irene Garousi-Nejad  <https://orcid.org/0000-0003-2929-3946>

David G. Tarboton  <https://orcid.org/0000-0002-1998-3479>

## REFERENCES

- Aalstad, K., Westermann, S., & Bertino, L. (2020). Evaluating satellite retrieved fractional snow-covered area at a high-Arctic site using terrestrial photography. *Remote Sensing of Environment*, 239, 111618. <https://doi.org/10.1016/j.rse.2019.111618>
- Anderson, E. A. (1976). *A point energy and mass balance model of a snow cover* (NOAA Technical Report No. NWS 29). National Weather Service. Retrieved from <https://repository.library.noaa.gov/view/noaa/6392>
- Barlage, M., Chen, F., Tewari, M., Ikeda, K., Gochis, D., Dudhia, J., Rasmussen, R., Livneh, B., Ek, M., & Mitchell, K. (2010). Noah land surface model modifications to improve snowpack prediction in the Colorado Rocky Mountains. *Journal of Geophysical Research*, 115(D22), D22101. <https://doi.org/10.1029/2009JD013470>
- Bennett, K. E., Cherry, J. E., Balk, B., & Lindsey, S. (2019). Using MODIS estimates of fractional snow cover area to improve streamflow forecasts in interior Alaska. *Hydrology and Earth System Sciences*, 23(5), 2439–2459. <https://doi.org/10.5194/hess-23-2439-2019>
- Bhatti, A. M., Koike, T., & Shrestha, M. (2016). Climate change impact assessment on mountain snow hydrology by water and energy budget-based distributed hydrological model. *Journal of Hydrology*, 543, 523–541. <https://doi.org/10.1016/j.jhydrol.2016.10.025>
- Chen, F., Barlage, M., Tewari, M., Rasmussen, R., Jin, J., Lettenmaier, D., Livneh, B., Lin, C., Miguez-Macho, G., Niu, G.-Y., Wen, L., & Yang, Z.-L. (2014). Modeling seasonal snowpack evolution in the complex terrain and forested Colorado headwaters region: A model intercomparison study. *Journal of Geophysical Research: Atmospheres*, 119(24), 13795–13819. <https://doi.org/10.1002/2014JD022167>
- Chen, F., Liu, C., Dudhia, J., & Chen, M. (2014). A sensitivity study of high-resolution regional climate simulations to three land surface models over the western United States. *Journal of Geophysical Research: Atmospheres*, 119(12), 7271–7291. <https://doi.org/10.1002/2014JD021827>
- Clow, D. W. (2010). Changes in the timing of snowmelt and streamflow in Colorado: A response to recent warming. *Journal of Climate*, 23(9), 2293–2306. <https://doi.org/10.1175/2009JCLI2951.1>
- Clow, D. W., Nanus, L., Verdin, K. L., & Schmidt, J. (2012). Evaluation of SNODAS snow depth and snow water equivalent estimates for the Colorado Rocky Mountains, USA. *Hydrological Processes*, 26(17), 2583–2591. <https://doi.org/10.1002/hyp.9385>
- Franz, K. J., Hogue, T. S., & Sorooshian, S. (2008). Operational snow modeling: Addressing the challenges of an energy balance model for National Weather Service forecasts. *Journal of Hydrology*, 360(1–4), 48–66. <https://doi.org/10.1016/j.jhydrol.2008.07.013>
- Garousi-Nejad, I., & Tarboton, D. (2022a). Data for a comparison of national water model retrospective analysis snow outputs at snotel sites across the Western U.S. *HydroShare* <https://www.hydroshare.org/resource/7a51f56c2cf24ae78012ac6a6d4815a6/>
- Garousi-Nejad, I., & Tarboton, D. (2022b). JavaScript code for retrieval of MODIS collection 6 NDSI snow cover at SNOTEL sites and a Jupyter

- Notebook to merge/reprocess data. *HydroShare* <https://www.hydroshare.org/resource/d287f010b2dd48edb0573415a56d47f8/>
- Garousi-Nejad, I., & Tarboton, D. (2022c). Notebook for retrieval of precipitation, air temperature, and snow water equivalent measurements at SNOTEL sites. *HydroShare* <https://www.hydroshare.org/resource/d1fe0668734e4892b066f198c4015b06/>
- Garousi-Nejad, I., & Tarboton, D. (2022d). Notebook to get the indices of National Water Model V2.0 grid cells containing SNOTL sites. *HydroShare* <https://www.hydroshare.org/resource/7839e3f3b4f54940bd3591b24803cacf/>
- Garousi-Nejad, I., & Tarboton, D. (2022e). Notebooks for combining the National Water Model results/inputs with observations from SNOTEL and MODIS at SNOTEL sites. *HydroShare* <https://www.hydroshare.org/resource/493e0ad05c2d45199427cc41a6c76de0/>
- Garousi-Nejad, I., & Tarboton, D. (2022f). Notebooks for post-processing the retrieved National Water Model V2.0 retrospective run results and inputs at SNOTEL sites. *HydroShare* <https://www.hydroshare.org/resource/1b66a752b0cc467eb0f46bda5fdc4b34/>
- Garousi-Nejad, I., & Tarboton, D. (2022g). Notebooks for visualizations reported at a comparison of national water model retrospective analysis snow outputs at snotel sites across the Western U.S. *HydroShare* <https://www.hydroshare.org/resource/8507aa41130e455fb0752026cf2253ab/>
- Gergel, D. R., Nijssen, B., Abatzoglou, J. T., Lettenmaier, D. P., & Stumbaugh, M. R. (2017). Effects of climate change on snowpack and fire potential in the western USA. *Climatic Change*, 141(2), 287–299. <https://doi.org/10.1007/s10584-017-1899-y>
- Gochis, D., Barlage, M., Cabell, R., Casali, M., Dugger, A., FitzGerald, K., McAllister, M., McCreight, J., RafieeiNasab, A., Read, L., Sampson, K., Yates, D., & Zhang, Y. (2020). The WRF-Hydro<sup>®</sup> modeling system technical description, (Version 5.1.1). NCAR Technical Note. Retrieved from <https://ral.ucar.edu/sites/default/files/public/WRFHydroV511TechnicalDescription.pdf>
- Gochis, D., Barlage, M., Cabell, R., Dugger, A., Fanfarillo, A., FitzGerald, K., McAllister, M., McCreight, J., RafieeiNasab, A., Read, L., Frazier, N., Johnson, D., Mattern, J. D., Karsten, L., Mills, T. J., & Fersch, B. (2020). WRF-Hydro<sup>®</sup> v5.1.1 (v5.1.1) [Computer software]. Zenodo. <https://doi.org/10.5281/ZENODO.3625238>
- Hall, D. K., & Riggs, G. A. (2016). MODIS/Terra snow cover daily L3 global 500m SIN grid [data set]. NASA National Snow and Ice Data Center DAAC. Retrieved from <https://doi.org/10.5067/MODIS/MOD10A1.006>
- Harder, P., & Pomeroy, J. W. (2014). Hydrological model uncertainty due to precipitation-phase partitioning methods. *Hydrological Processes*, 28(14), 4311–4327. <https://doi.org/10.1002/hyp.10214>
- Hedstrom, N. R., & Pomeroy, J. W. (1998). Measurements and modelling of snow interception in the boreal forest. *Hydrological Processes*, 12, 1611–1625. [https://doi.org/10.1002/\(SICI\)1099-1085\(199808/09\)12:10<11%3C1611::AID-HYP684%3E3.0.CO;2-4](https://doi.org/10.1002/(SICI)1099-1085(199808/09)12:10<11%3C1611::AID-HYP684%3E3.0.CO;2-4)
- Helbig, N., van Herwijnen, A., Magnusson, J., & Jonas, T. (2015). Fractional snow-covered area parameterization over complex topography. *Hydrology and Earth System Sciences*, 19(3), 1339–1351. <https://doi.org/10.5194/hess-19-1339-2015>
- Horritt, M. S., & Bates, P. D. (2002). Evaluation of 1D and 2D numerical models for predicting river flood inundation. *Journal of Hydrology*, 268(1–4), 87–99. [https://doi.org/10.1016/S0022-1694\(02\)00121-X](https://doi.org/10.1016/S0022-1694(02)00121-X)
- Hou, D., Charles, M., Luo, Y., Toth, Z., Zhu, Y., Krzysztofowicz, R., Lin, Y., Xie, P., Seo, D.-J., Pena, M., & Cui, B. (2014). Climatology-calibrated precipitation analysis at fine scales: Statistical adjustment of stage IV toward CPC gauge-based analysis. *Journal of Hydrometeorology*, 15(6), 2542–2557. <https://doi.org/10.1175/JHM-D-11-0140.1>
- Jordan, R. E. (1991). A one-dimensional temperature model for a snow cover: Technical documentation for SNTherm.89. Cold Regions Research and Engineering Laboratory (U.S.). Retrieved from <http://hdl.handle.net/11681/11677>
- Lahmers, T. M., Gupta, H., Castro, C. L., Gochis, D. J., Yates, D., Dugger, A., Goodrich, D., & Hazenberg, P. (2019). Enhancing the structure of the WRF-hydro hydrologic model for semiarid environments. *Journal of Hydrometeorology*, 20(4), 691–714. <https://doi.org/10.1175/JHM-D-18-0064.1>
- Li, D., Wrzesien, M. L., Durand, M., Adam, J., & Lettenmaier, D. P. (2017). How much runoff originates as snow in the western United States, and how will that change in the future?: Western U.S. snowmelt-derived runoff. *Geophysical Research Letters*, 44(12), 6163–6172. <https://doi.org/10.1002/2017GL073551>
- Livneh, B., & Badger, A. M. (2020). Drought less predictable under declining future snowpack. *Nature Climate Change*, 10(5), 452–458. <https://doi.org/10.1038/s41558-020-0754-8>
- Livneh, B., Xia, Y., Mitchell, K. E., Ek, M. B., & Lettenmaier, D. P. (2010). Noah LSM snow model diagnostics and enhancements. *Journal of Hydrometeorology*, 11(3), 721–738. <https://doi.org/10.1175/2009JHM1174.1>
- Loth, B., Graf, H.-F., & Oberhuber, J. M. (1993). Snow cover model for global climate simulations. *Journal of Geophysical Research*, 98(D6), 10451. <https://doi.org/10.1029/93JD00324>
- Lundquist, J. D., & Flint, A. L. (2006). Onset of snowmelt and Streamflow in 2004 in the Western United States: How shading may affect spring streamflow timing in a warmer world. *Journal of Hydrometeorology*, 7(6), 1199–1217. <https://doi.org/10.1175/JHM539.1>
- Lynch-Stieglitz, M. (1994). The development and validation of a simple snow model for the GISS GCM. *Journal of Climate*, 7(12), 1842–1855. <http://www.jstor.org/stable/26198671>
- Magand, C., Ducharne, A., Le Moine, N., & Gascoïn, S. (2014). Introducing hysteresis in snow depletion curves to improve the water budget of a land surface model in an alpine catchment. *Journal of Hydrometeorology*, 15(2), 631–649. <https://doi.org/10.1175/JHM-D-13-091.1>
- Mahat, V., & Tarboton, D. G. (2014). Representation of canopy snow interception, unloading and melt in a parsimonious snowmelt model. *Hydrological Processes*, 28(26), 6320–6336. <https://doi.org/10.1002/hyp.10116>
- Masson, T., Dumont, M., Mura, M., Sirguey, P., Gascoïn, S., Dedieu, J.-P., & Chanussot, J. (2018). An assessment of existing methodologies to retrieve snow cover fraction from MODIS data. *Remote Sensing*, 10(4), 619. <https://doi.org/10.3390/rs10040619>
- McCreight, J. L., Small, E. E., & Larson, K. M. (2014). Snow depth, density, and SWE estimates derived from GPS reflection data: Validation in the western U.S. *Water Resources Research*, 50(8), 6892–6909. <https://doi.org/10.1002/2014WR015561>
- McEnery, J., Ingram, J., Duan, Q., Adams, T., & Anderson, L. (2005). NOAA'S advanced hydrologic prediction service: Building pathways for better science in water forecasting. *Bulletin of the American Meteorological Society*, 86(3), 375–386. <https://doi.org/10.1175/BAMS-86-3-375>
- Meyer, J. D. D., Jin, J., & Wang, S.-Y. (2012). Systematic patterns of the inconsistency between snow water equivalent and accumulated precipitation as reported by the snowpack telemetry network. *Journal of Hydrometeorology*, 13(6), 1970–1976. <https://doi.org/10.1175/JHM-D-12-066.1>
- Mote, P. W. (2003). Trends in snow water equivalent in the Pacific Northwest and their climatic causes. *Geophysical Research Letters*, 30(12), 1601. <https://doi.org/10.1029/2003GL017258>
- Mote, P. W., Hamlet, A. F., Clark, M. P., & Lettenmaier, D. P. (2005). Declining mountain snowpack in Western North America\*. *Bulletin of the American Meteorological Society*, 86(1), 39–50. <https://doi.org/10.1175/BAMS-86-1-39>
- Naple, P., Letcher, T., Minder, J. R., Gochis, D., Dugger, A., & RafieeiNasab, A. (2020). Improving parameterizations of snow in the National Water Model with observations from the New York State Mesonet to better simulate snow and streamflow in the northeastern

- United States. AGU Fall Meeting, Virtual. Retrieved from <https://ui.adsabs.harvard.edu/abs/2020AGUFMC063.0006N/abstract>
- National Research Council. (2006). *Toward a new advanced hydrologic prediction service (AHPs)*. National Academies Press. <https://doi.org/10.17226/11598>
- National Weather Service. (2019). National-water-model-V2. *Google Cloud Bucket*. Retrieved from <https://console.cloud.google.com/storage/browser/national-water-model-v2>
- Niu, G.-Y., & Yang, Z.-L. (2004). Effects of vegetation canopy processes on snow surface energy and mass balances. *Journal of Geophysical Research: Atmospheres*, 109(D23), D23111. <https://doi.org/10.1029/2004JD004884>
- Niu, G.-Y., & Yang, Z.-L. (2007). An observation-based formulation of snow cover fraction and its evaluation over large North American river basins. *Journal of Geophysical Research*, 112(D21), D21101. <https://doi.org/10.1029/2007JD008674>
- Niu, G.-Y., Yang, Z.-L., Mitchell, K. E., Chen, F., Ek, M. B., Barlage, M., Kumar, A., Manning, K., Niyogi, D., Rosero, E., Tewari, M., & Xia, Y. (2011). The community Noah land surface model with multiparameterization options (Noah-MP): 1. Model description and evaluation with local-scale measurements. *Journal of Geophysical Research*, 116(D12), D12109. <https://doi.org/10.1029/2010JD015139>
- Omernik, J. M., & Griffith, G. E. (2014). Ecoregions of the conterminous United States: Evolution of a hierarchical spatial framework. *Environmental Management*, 54(6), 1249–1266. <https://doi.org/10.1007/s00267-014-0364-1>
- Pan, M., Sheffield, J., Wood, E. F., Mitchell, K. E., Houser, P. R., Schaake, J. C., Robock, A., Lohmann, D., Cosgrove, B., Duan, Q., Luo, L., Higgins, R. W., Pinker, R. T., & Tarpley, J. D. (2003). Snow process modeling in the North American Land Data Assimilation System (NLDA5): 2. Evaluation of model simulated snow water equivalent. *Journal of Geophysical Research: Atmospheres*, 108(D22), 2003JD003994. <https://doi.org/10.1029/2003JD003994>
- RafieeiNasab, A., Karsten, L., Dugger, A., FitzGerald, K., Cabell, R., Gochis, D., Yates, D., Sampson, K., McCreight, J., Read, L., Zhang, Y., & McAllister, M. (2020). *Overview of National Water Model calibration general strategy & optimization, NCAR Community WRF-Hydro Modeling System training workshop*. NCAR Community WRF-Hydro Modeling System training workshop. Retrieved from [https://ral.ucar.edu/projects/wrf\\_hydro/training-materials](https://ral.ucar.edu/projects/wrf_hydro/training-materials)
- Regonda, S. K., Rajagopalan, B., Clark, M., & Pitlick, J. (2005). Seasonal cycle shifts in hydroclimatology over the Western United States. *Journal of Climate*, 18(2), 372–384. <https://doi.org/10.1175/JCLI-3272.1>
- Riggs, G. A., Hall, D. K., & Román, M. O. (2016). *MODIS snow products collection 6 user guide*. Retrieved from [http://modis-snow-ice.gsfc.nasa.gov/uploads/C6\\_MODIS\\_Snow\\_User\\_Guide.pdf](http://modis-snow-ice.gsfc.nasa.gov/uploads/C6_MODIS_Snow_User_Guide.pdf)
- Riggs, G. A., Hall, D. K., & Román, M. O. (2017). Overview of NASA's MODIS and visible infrared imaging radiometer suite (VIIRS) snow-cover earth system data records. *Earth System Science Data*, 9(2), 765–777. <https://doi.org/10.5194/essd-9-765-2017>
- Salomonson, V. V., & Appel, I. (2006). Development of the aqua MODIS NDSI fractional snow cover algorithm and validation results. *IEEE Transactions on Geoscience and Remote Sensing*, 44(7), 1747–1756. <https://doi.org/10.1109/TGRS.2006.876029>
- Sangwan, N., & Merwade, V. (2015). A faster and economical approach to floodplain mapping using soil information. *Journal of the American Water Resources Association*, 51(5), 1286–1304. <https://doi.org/10.1111/1752-1688.12306>
- Shamir, E., Carpenter, T. M., Fickenscher, P., & Georgakakos, K. P. (2006). Evaluation of the National Weather Service operational hydrologic model and forecasts for the American River Basin. *Journal of Hydrologic Engineering*, 11(5), 392–407. [https://doi.org/10.1061/\(ASCE\)1084-0699\(2006\)11:5\(392\)](https://doi.org/10.1061/(ASCE)1084-0699(2006)11:5(392))
- Steele, C., Dialesandro, J., James, D., Elias, E., Rango, A., & Bleiweiss, M. (2017). Evaluating MODIS snow products for modelling snowmelt runoff: Case study of the Rio Grande headwaters. *International Journal of Applied Earth Observation and Geoinformation*, 63, 234–243. <https://doi.org/10.1016/j.jag.2017.08.007>
- Stewart, I. T., Cayan, D. R., & Dettinger, M. D. (2004). Changes in snowmelt runoff timing in Western North America under a 'business as usual' climate change scenario. *Climatic Change*, 62(1–3), 217–232. <https://doi.org/10.1023/B:CLIM.0000013702.22656.e8>
- Stewart, I. T., Cayan, D. R., & Dettinger, M. D. (2005). Changes toward earlier streamflow timing across Western North America. *Journal of Climate*, 18(8), 1136–1155. <https://doi.org/10.1175/JCLI3321.1>
- Sun, N., Yan, H., Wigmosta, M. S., Leung, L. R., Skaggs, R., & Hou, Z. (2019). Regional snow parameters estimation for large-domain hydrological applications in the Western United States. *Journal of Geophysical Research: Atmospheres*, 124(10), 5296–5313. <https://doi.org/10.1029/2018JD030140>
- Swenson, S. C., & Lawrence, D. M. (2012). A new fractional snow-covered area parameterization for the community land model and its effect on the surface energy balance. *Journal of Geophysical Research: Atmospheres*, 117(D21), n/a-n/a. <https://doi.org/10.1029/2012JD018178>
- Tarboton, D., & Garousi-Nejad, I. (2022). Notebook for retrieval of National Water Model V2.0 Retrospective run results at SNOTEL sites. *HydroShare* <https://www.hydroshare.org/resource/3d4976bf6eb84dfbbe11446ab0e31a0a/>
- Toure, A. M., Rodell, M., Yang, Z.-L., Beaudoin, H., Kim, E., Zhang, Y., & Kwon, Y. (2016). Evaluation of the snow simulations from the community land model, version 4 (CLM4). *Journal of Hydrometeorology*, 17(1), 153–170. <https://doi.org/10.1175/JHM-D-14-0165.1>
- Towns, J., Cockerill, T., Dahan, M., Foster, I., Gaither, K., Grimshaw, A., Hazlewood, V., Lathrop, S., Lifka, D., Peterson, G. D., Roskies, R., Scott, J. R., & Wilkins-Diehr, N. (2014). XSEDE: Accelerating scientific discovery. *Computing in Science & Engineering*, 16(5), 62–74. <https://doi.org/10.1109/MCSE.2014.80>
- Trujillo, E., & Molotch, N. P. (2014). Snowpack regimes of the Western United States. *Water Resources Research*, 50(7), 5611–5623. <https://doi.org/10.1002/2013WR014753>
- US Department of Agriculture. (2011). *Snow survey and water supply forecasting*. *National Engineering Handbook Part 622*. Water and Climate Center, Natural Resources Conservation Service. Retrieved from <https://directives.sc.egov.usda.gov/viewerFS.aspx?hid=32040>
- Viterbo, F., Mahoney, K., Read, L., Salas, F., Bates, B., Elliott, J., Cosgrove, B., Dugger, A., Gochis, D., & Cifelli, R. (2020). A multiscale, hydrometeorological forecast evaluation of National Water Model Forecasts of the May 2018 Ellicott City, Maryland, Flood. *Journal of Hydrometeorology*, 21(3), 475–499. <https://doi.org/10.1175/JHM-D-19-0125.1>
- Wang, X., Zhu, Y., Chen, Y., Zheng, H., Liu, H., Huang, H., Liu, K., & Liu, L. (2017). Influences of forest on MODIS snow cover mapping and snow variations in the Amur River basin in Northeast Asia during 2000–2014. *Hydrological Processes*, 31(18), 3225–3241. <https://doi.org/10.1002/hyp.11249>
- Wang, Y., Broxton, P., Fang, Y., Behrangi, A., Barlage, M., Zeng, X., & Niu, G. (2019). A wet-bulb temperature-based rain-snow partitioning scheme improves snowpack prediction over the drier Western United States. *Geophysical Research Letters*, 46(23), 13825–13835. <https://doi.org/10.1029/2019GL085722>
- Wrzesien, M. L., Pavelsky, T. M., Kapnick, S. B., Durand, M. T., & Painter, T. H. (2015). Evaluation of snow cover fraction for regional climate simulations in the Sierra Nevada. *International Journal of Climatology*, 35(9), 2472–2484. <https://doi.org/10.1002/joc.4136>
- Yang, Z.-L., & Dickinson, R. E. (1996). Description of the biosphere-atmosphere transfer scheme (BATS) for the soil moisture workshop and evaluation of its performance. *Global and Planetary Change*, 13(1–4), 117–134. [https://doi.org/10.1016/0921-8181\(95\)00041-0](https://doi.org/10.1016/0921-8181(95)00041-0)

- Yang, Z.-L., Niu, G.-Y., Mitchell, K. E., Chen, F., Ek, M. B., Barlage, M., Longuevergne, L., Manning, K., Niyogi, D., Tewari, M., & Xia, Y. (2011). The community Noah land surface model with multiparameterization options (Noah-MP): 2. Evaluation over global river basins. *Journal of Geophysical Research*, 116(D12), D12110. <https://doi.org/10.1029/2010JD015140>
- You, J., Tarboton, D. G., & Luce, C. H. (2014). Modeling the snow surface temperature with a one-layer energy balance snowmelt model. *Hydrology and Earth System Sciences*, 18(12), 5061–5076. <https://doi.org/10.5194/hess-18-5061-2014>
- Zalenski, G., Krajewski, W. F., Quintero, F., Restrepo, P., & Buan, S. (2017). Analysis of National Weather Service Stage forecast errors. *Weather and Forecasting*, 32(4), 1441–1465. <https://doi.org/10.1175/WAF-D-16-0219.1>
- Zhang, J., Condon, L. E., Tran, H., & Maxwell, R. M. (2021). A national topographic dataset for hydrological modeling over the contiguous United States. *Earth System Science Data*, 13(7), 3263–3279. <https://doi.org/10.5194/essd-13-3263-2021>

**How to cite this article:** Garousi-Nejad, I., & Tarboton, D. G. (2022). A comparison of National Water Model retrospective analysis snow outputs at snow telemetry sites across the Western United States. *Hydrological Processes*, 36(1), e14469. <https://doi.org/10.1002/hyp.14469>